Evaluation of cloud microphysics schemes in simulations of a winter storm using radar and radiometer measurements

Mei Han,[1,2] Scott A. Braun,[2] Toshihisa Matsui,[2,3] and Christopher R. Williams[4,5]

Received 18 June 2012; revised 12 October 2012; accepted 30 November 2012; published 14 February 2013.

[1] Using observations from a space-borne radiometer and a ground-based precipitation profiling radar, the impact of cloud microphysics schemes in the WRF model on the simulation of microwave brightness temperature (T_b), radar reflectivity, and Doppler velocity (V_{dop}) is studied for a winter storm in California. The unique assumptions of particles size distributions, number concentrations, shapes, and fall speeds in different microphysics schemes are implemented into a satellite simulator and customized calculations for the radar are performed to ensure consistent representation of precipitation properties between the microphysics schemes and the radiative transfer models.

[2] Simulations with four different schemes in the WRF model, including the Goddard scheme (GSFC), the WRF single-moment 6-class scheme (WSM6), the Thompson scheme (THOM), and the Morrison double-moment scheme (MORR), are compared directly with measurements from the sensors. Results show large variations in the simulated radiative properties. General biases of ~20 K or larger are found in (polarization-corrected) T_b, which is linked to an overestimate of the precipitating ice aloft. The simulated reflectivity with THOM appears to agree well with the observations, while high biases of ~5−10 dBZ are found in GSFC, WSM6 and MORR. Peak reflectivity in MORR exceeds other schemes. These biases are attributable to the snow intercept parameters or the snow number concentrations. Simulated V_{dop} values based on GSFC agree with the observations well, while other schemes appear to have a ~1 m s^{-1} high bias in the ice layer. In the rain layer, the model representations of Doppler velocity vary at different sites.

Citation: Han, M., S. A. Braun, T. Matsui, and C. R. Williams (2013), Evaluation of cloud microphysics schemes in simulations of a winter storm using radar and radiometer measurements, *J. Geophys. Res. Atmos.*, *118*, 1401–1419, doi:10.1002/jgrd.50115.

1. Introduction

[3] Numerous cloud microphysical schemes have been developed in numerical weather prediction (NWP) models to account for the complicated nature of cloud and precipitation systems. For example, the Weather Research and Forecasting (WRF) model provides more than a dozen options of cloud microphysics schemes with different degrees of sophistication [e.g., *Lin et al*., 1983; *Tao and Simpson*, 1993; *Ferrier*, 1994; *Morrison et al*., 2005 and 2009; *Milbrandt and Yau*, 2005; *Hong and Lim*, 2006; *Thompson et al*., 2008; *Lin and Colle*, 2011]. These schemes may fundamentally vary in the categories of hydrometeor species and the number of moments in their prognostic variables (e.g., if both mass and number of hydrometeors species are predicted). In addition, the schemes could also differ in many other ways, including particle size distributions (PSDs), particle shapes, mass-diameter relationships, particle fall speed assumptions, and treatments for microphysical processes, such as autoconversion and collision/coalescence. These variations result in differences in the prediction of precipitation vertical profiles and surface accumulations [e.g., *Liu et al*., 2011; *Molthan and Colle*, 2012]. They also produce differences in simulated remote sensing measurements of cloud and precipitation systems [e.g., *Matsui et al*., 2009; *Han et al*., 2010; *Tao et al*., 2011; *Lang et al*., 2011; *Molthan and Colle*, 2012].

[4] Since in-situ microphysics observations are often limited in space and time, remote sensing data obtained from instruments in space, on aircraft, and on the ground are widely used to validate model simulations. In particular, active and passive microwave instruments (i.e., radar and radiometer) offer great capabilities for characterizing profiles of cloud and precipitation species in the atmosphere. In this paper, we will use observations from a passive sensor, the Advanced Microwave Scanning Radiometer for EOS (AMSR-E) onboard the Aqua satellite. It observes microwave radiances emitted and scattered from the Earth's surface and atmosphere. The high frequency channel

[1]Goddard Earth Sciences Technology and Research, Morgan State University, Baltimore, Maryland, USA.
[2]Mesoscale Atmospheric Process Laboratory, NASA Goddard Space Flight Center, Greenbelt, Maryland, USA.
[3]ESSIC, University of Maryland, College Park, Maryland, USA.
[4]Cooperative Institute for Research in Environmental Sciences, University of Colorado, Boulder, Colorado, USA.
[5]NOAA Earth System Research Laboratory, Boulder, Colorado, USA.

Corresponding author: M. Han, Mesoscale Atmospheric Process Laboratory, NASA GSFC, Code 612, Greenbelt, MD 20771. (Mei.Han@nasa.gov)

2169-897X/13/10.1002/jgrd.50115

(89 GHz) is sensitive to scattering processes by precipitation ice species and provides a horizontal snapshot of precipitation at fairly high spatial resolution [~5 km Effective Field of View (EFOV)] nearly twice a day. In addition, measurements from an active sensor, the ground-based S-band (2875 MHz) vertical pointing Doppler radar [S-PROF, *Williams et al*., 2007], are analyzed. The radar detects the microwave energy backscattered by precipitation particles and observes the vertical structure of the precipitation system, including the reflectivity and the Doppler velocity.

[5] When NWP model simulations are evaluated against observations obtained by any passive or active microwave instrument, assumptions regarding microphysical properties of clouds and precipitation that influence calculations in both NWP and radiative transfer models must be consistent. Here, to the extent possible, we implement the same microphysics assumptions from the WRF model into the Goddard Satellite Data Simulator Unit [G-SDSU, *Matsui et al*., 2009 and *Masunaga et al*., 2010] in order to simulate the AMSR-E-observed radiance. We also develop customized calculations of the radar observations for the ground-based S-band profiler, including both radar reflectivity and Doppler velocity.

[6] This methodology of integrating a NWP model with a forward radiative transfer model has recently been used to evaluate model simulations and to improve model microphysics schemes [e.g., *Matsui et al*., 2009; *Han et al*., 2010; *Li et al*., 2010; *Shi et al*., 2010]. It is also one of the key components in algorithm development to retrieve or assimilate remote sensing data [e.g., *Olson et al*., 2001; *Tong and Xue*, 2005; *Zupanski et al*., 2011; *Blahak et al*., 2011]. Our research efforts mainly focus on model evaluation and improvement. *Han et al*. [2010] demonstrated the merit of using both the radar and radiometer onboard the TRMM satellite to study precipitation structure and to evaluate the performance of five single-moment bulk microphysics schemes in the fifth-generation Pennsylvania State University-National Center for Atmospheric Research Mesoscale Model (MM5). In this paper, we continue such work by assessing four microphysics schemes in the WRF model for a wintertime precipitation system over land, including both single and double moment microphysics schemes. The paper is organized as follows. Section 2 introduces the WRF model configuration and the microphysics schemes. It also describes the multi-instrument satellite simulator and the methodology for simulating the radar reflectivity and the Doppler velocity of the S-band profiling radar. Section 3 describes the case and the observations obtained by the radiometer and the radar. Model simulations of hydrometeor vertical profiles, brightness temperatures, radar reflectivity, and Doppler velocities are analyzed in section 4. Conclusions and discussion follow in section 5.

2. Models and Calculations

a. Configurations and microphysics schemes in the WRF model

[7] The Advance Research WRF model Version 3.1 is used to conduct four simulations from 0000 UTC 30 December 2005 to 0000 UTC 1 January 2006. The model grids consist of 52 vertical levels and 4 two-way interactive nested domains with the highest horizontal grid spacing of 1.3 km. The NCEP FNL (Final) Operational Model Global Tropospheric Analyses with $1^\circ \times 1^\circ$ horizontal and 6-h temporal resolution are used to provide the initial and lateral boundary conditions. The WRF model outputs are saved every 5 minutes. The simulation with the Morrison microphysics scheme uses a monotonic advection option for moisture variables, while the others use the positive-definite advection option. Other than the choice of different microphysics schemes and advection scheme, model configurations are identical among all model simulations.

[8] The four microphysical schemes investigated in this paper include the Goddard bulk single-moment scheme [hereinafter GSFC, *Tao and Simpson*, 1993; *Tao et al*., 2003; *Lang et al*., 2007], the WRF single-moment 6-class scheme [hereinafter WSM6, [*Hong and Lim*, 2006], the Thompson scheme [hereinafter THOM, *Thompson et al*., 2008], and the Morrison double-moment scheme [hereinafter MORR, *Morrison et al*., 2005; *Morrison et al*., 2009]. Each scheme assumes six categories of water species: water vapor, cloud water, cloud ice, snow, graupel, and rain. Because the observations used in this study are mainly sensitive to precipitation species, we will focus our analysis on snow, graupel, and rain (see Table 1 for their PSD assumptions, etc.). The single-moment schemes, GSFC and WSM6, only predict mass mixing ratios of the precipitation species. THOM adds another moment for rain, i.e., the number concentration, as a prognostic variable. MORR is a full double-moment scheme, predicting both mass mixing ratios and number concentrations for the three precipitation species.

[9] The PSDs of most precipitation species in the four schemes adopt a generalized-gamma distribution function, with the exception of snow in THOM. The generalized-gamma distribution function is:

Table 1. PSD, Shape, and Density Assumptions for Precipitation Hydrometeor Species

Two Moment Species		PSD						M-D (If spheres?)			Bulk Density (kg m^{-3})		
		μ			N_0 (m^{-4})								
		Sn	Gr	Ra	Sn	Gr	Ra	Sn	Gr	Ra	Sn	Gr	Ra
GSFC	NA	0	0	0	1.6×10^7	$4.\times10^6$	$8.\times10^6$	Y	Y	Y	100.	400.	1000.
WSM6	NA	0	0	0	$N_{0s}(T)$	$4.\times10^6$	$8.\times10^6$	Y	Y	Y	100.	500.	1000.
THOM	rain	NA	0	0	NA	$N_{0g}(q)$	$N_{0r}(n,q)$	N	Y	Y	not a const.	400.	1000.
MORR	rain, snow, graupel	0	0	0	$N_{0s}(n,q)$	$N_{0g}(n,q)$	$N_{0r}(n,q)$	Y	Y	Y	100.	400.	997.

Note: See Eq. 2 and relevant text for the assumptions for snow in THOM.

$$N_x(D) = N_{0_x} D^{\mu_x} e^{-\lambda_x D}, \quad (1)$$

where x represents snow, graupel, or rain; N_{0x} (m^{-4}) is the intercept parameter; μ_x is the shape factor for the gamma function; and λ_x (m^{-1}) is the slope parameter for species x. $N(D)dD$ (m^{-3} m) is the number of particles per unit volume with diameters between D and $D+dD$. The four schemes differ in the way the intercept parameters are specified (Table 1). GSFC uses constants for N_{0x} while WSM6 uses a temperature dependent method for N_{0s} and constants for N_{0r} and N_{0g}. THOM and MORR diagnose the N_{0x} with the predicted mixing ratio and/or number concentrations. It should also be noted that the implementation of the gamma distribution function in the different schemes varies. For example, GSFC, WSM6, and MORR do not implement the shape factor in their codes for precipitation species. THOM implements the shape factors, but with μ_g and μ_r set to zero by default. Therefore, the distribution of almost every precipitation species in the four schemes is represented with an exponential function (The terms "gamma" and "exponential" will be used alternatively in this paper for convenience.). The exception is snow in THOM whose PSD follows

$$N(D) = \frac{M_2^4}{M_3^3}\left[\kappa_0 e^{-\frac{M_2}{M_3}\Lambda_0 D} + \kappa_1 \left(\frac{M_2}{M_3} D\right)^{\mu_s} e^{-\frac{M_2}{M_3}\Lambda_1 D}\right], \quad (2)$$

where $M_n = \int D^n N(D) dD$ is the n^{th} moment of the distribution [See *Thompson et al*. [2008] and *Field et al*. [2005] for the definition of other parameters].

[10] The shapes of the precipitation particles and the particles' mass-diameter relationships (m-D) are also important factors in the model representation of precipitation species. Almost all of the precipitation species in the four schemes are assumed to be spheres, with the exception of snow in THOM that is assumed to be fractal-like aggregates. The general form of the m-D relationship is

$$m_x(D) = c_x D^{d_x}, \quad (3)$$

where $c_x = \pi\rho_x/6$, $d_x = 3$ for spheres, and ρ_x is the bulk density for species x. Snow in THOM uses

$$m(D) = 0.069 D^2. \quad (4)$$

[11] Furthermore, to describe parameters that are important in calculating the brightness temperature, radar reflectivity and Doppler velocity, we derive the formula for the intercept (N_{0x}) and slope (λ_x) parameters for the precipitation species with gamma PSD in the four schemes (i.e., except snow in THOM). The derivation starts from the definition of water content ($\rho_a q_x$, kg m^{-3}), i.e., $\rho_a q_x = \int N_x(D) m_x(D) dD$, where ρ_a is the air density and q_x is the mixing ratio of species x. Because all of the species are assumed to be spheres with constant bulk density, and their PSDs are actually simplified exponential functions, we categorize the species into two groups based on whether the number concentration is predicted. The first category is for single-moment species (including snow, graupel, and rain in both the GSFC and WSM6 schemes and graupel in the THOM scheme). Their N_{0x} is either fixed or prescribed as a function of temperature or mixing ratio (Table 1). The slope parameter for these species is derived as:

$$\lambda_x = \left(\frac{\pi\rho_x N_{0x}}{\rho_a q_x}\right)^{1/4}. \quad (5)$$

The second category is for double-moment species (including rain in the THOM scheme; snow, graupel, and rain in the MORR scheme). Their intercept and slope parameters are:

$$N_{0x} = N_x \lambda_x \quad (6)$$

$$\lambda_x = \left(\frac{\pi\rho_x N_x}{\rho_a q_x}\right)^{1/3}, \quad (7)$$

where the model prognostic variable N_x is used in the calculation.

b. Calculations of brightness temperature using the G-SDSU

[12] The Goddard Satellite Data Simulation Unit [G-SDSU, *Matsui et al*. 2009; *Masunaga et al*., 2010] is used to simulate microwave brightness temperatures from the WRF output. The G-SDSU is a package of forward radiative transfer models that is capable of simulating satellite-observed radiance and backscattered signals from cloud-system resolving model output at multiple observational frequencies for sensors onboard a wide variety of satellites. The G-SDSU simulation unit takes the following WRF simulation variables as input: profiles of the pressure, temperature, water vapor, geopotential height, cloud and precipitation hydrometeors' mass mixing ratios (and number concentrations for MORR) to calculate atmospheric single-scattering properties; and surface properties including surface skin temperature, land cover (water or land), surface wind speed, vegetation cover, soil moisture, and snow depth to calculate surface emissivity and boundary conditions in radiative transfer models. The passive microwave radiative transfer calculation for cloud and precipitation was developed based on the two-stream radiative transfer with the delta Eddington assumption [*Kummerow*, 1993; *Olson et al*., 2001]. The single-scattering properties are computed via Lorenz-Mie solution with Maxwell-Garnett effective refractive index. To ensure consistency between the WRF model and the radiative transfer calculations, the G-SDSU utilizes identical assumptions regarding microphysical properties of hydrometeor species in the GSFC, WSM6, and MORR schemes as described in the previous subsection. However, the PSD assumption of THOM is not included in G-SDSU. Instead, the GSFC PSD assumptions are used in the THOM T_b calculations to simplify code implementation.

[13] Since high frequency channels of passive microwave sensors are particularly sensitive to precipitation species (mostly precipitating ice aloft) over land, we focus on analyzing observations obtained by AMSR-E at 89 GHz. AMSR-E detects the depression of brightness temperatures caused by the reduction of earth-emitted/reflected microwave radiation being scattered by frozen precipitation hydrometeors. If low-emissivity water bodies coexist with high-emissivity land surfaces in the same scene, ambiguities arise when interpreting the low brightness temperature due

to precipitation scattering. Therefore, a linear transformation of the dual-polarization brightness temperatures at 89 GHz, i.e. the Polarization-Corrected Temperature [PCT, *Spencer et al*., 1989] is used in this paper to mask out the surface variability of microwave brightness temperature. The PCT at 89 GHz is defined as $PCT89 = 1.82T_{B_v} - 0.82T_{B_h}$, where T_{B_v} and T_{B_h} are brightness temperatures at vertical and horizontal polarization, respectively. The observed and simulated PCT will be presented in sections 3 and 4.

c. Calculations of equivalent radar reflectivity factor (Z_e) from WRF model output

[14] Methods to calculate equivalent radar reflectivity factor Z_e from model-derived microphysical properties have been described in the literature [e.g. *Smith*, 1984; *Ferrier*, 1994; *Hogan et al*., 2006; *Milbrandt et al*., 2008]. Because this study will investigate both the simulated Z_e and the Doppler velocity, we begin with the strict definition of radar reflectivity as the *sum of the backscattering cross section (σ) in a unit volume*, $\eta = \int \sigma N(D) dD$. The equivalent radar reflectivity factor (Z_e, $m^6 m^{-3}$ in SI units) is chosen to characterize radar reflectivity (η, $m^2 m^{-3}$ in SI unit) to account for different hydrometeor backscattering cross sections occurring in the same radar sampling volume. See Appendix A for the derivation of Z_e (Eqs. A.6 and A.7) for the four microphysics schemes with multiple species and under the Rayleigh approximation.

d. Calculations of Doppler velocity from the WRF model

[15] The Doppler velocity observed by the vertically pointing radar represents the sum of the hydrometeors' terminal velocities and the vertical air motion, weighted by the reflectivity (η). In contrast, NWP models predict hydrometeors' vertical flux and only calculate mass-weighted terminal velocities. In order to simulate Doppler velocities (V_{dop}) that can be compared to the observations, we write

$$V_{dop} = V_\eta + w, \tag{8}$$

where w is the vertical air motion. The reflectivity weighted terminal velocity, V_η, includes contributions from all precipitation species:

$$V_\eta = \frac{\sum_{x=1}^{n} \int \sigma_x(D) v_x(D) N_x(D) dD}{\sum_{x=1}^{n} \int \sigma_x(D) N_x(D) dD}, \tag{9}$$

where $n = 3$ and x stands for snow, graupel, and rain. Similar approaches were developed for other numerical models [*Caumont and Ducrocq*, 2008; *Blahak et al*., 2011]. The PSD and backscattering cross section (σ_x) follow the definitions in sections 2c and APPENDIX A. We use a generalized formula for the particle fall speed,

$$v_x(D) = a_x D^{b_x} e^{-f_x D} \left(\frac{\rho_0}{\rho}\right)^{c_v}, \tag{10}$$

where a_x and b_x are determined from observations at a reference level (with air density of ρ_0), usually at the ground [e.g. *Locatelli and Hobbs*, 1974] for species x. The factor $(\rho_0/\rho)^{c_v}$ corrects the ground-level fall speed to upper levels where air density is ρ [*Foote and du Toit*, 1969]. Only THOM introduces the exponential factor for rain and snow following *Ferrier* [1994]. See Table 2 for details about these parameters used in the four microphysics schemes. See APPENDIX B for the equations for V_η for the four schemes.

3. Event Description and Observations

[16] On December 30–31, 2005, a landfalling winter cyclone caused intense precipitation and flooding in the mountain and valley regions of northern California and Nevada. This system was characterized by a strong prefrontal low-level jet (LLJ) that transported abundant moisture onshore in the cyclone's warm sector. The moisture-laden LLJ is often referred to as an "Atmospheric River (AR)" and is readily observed by water vapor channels in microwave radiometers [e.g., *Neiman et al*., 2008; *Ralph et al*., 2011]. *Smith et al*., [2010] documented the synoptic environment and moisture fluxes for the atmospheric river discussed in the current study.

[17] This storm was sampled by the NASA Aqua satellite and a wide variety of ground-based instruments deployed by the NOAA Hydrometeorological Testbed (HMT) program. Here, we analyze the structure of the precipitation as observed by AMSR-E and S-PROF. The AMSR-E instrument calibration and data (Level 2A brightness temperature)

Table 2. Constants and/or Variables for Fall Speeds of Precipitation Species

		GSFC	WSM6	MORR	THOM
Rain	a_r	841.9	841.9	841.9	4854
	b_r	0.8	0.8	0.8	1
	f_r	0	0	0	195
Snow	a_s	1.30493	11.72	11.72	40
	b_s	0.11	0.41	0.41	0.55
	f_s	0	0	0	125
Graupel	a_g	19.3	330.	19.3	442
	b_g	0.37	0.8	0.37	0.89
	f_g	0	0	0	0
Reference density	ρ_0	Variable air density at 2nd lowest model level	1.28	1.18 (a constant air density at 1013 hPa and 25° C)	1.08 (a constant air density at 850 hPa and 0° C)
Density adjustment exponent	c_v	0.5	0.5	0.54	0.5

quality control can be found in *Ashcroft and Wentz* [2006]. The S-PROF radars were deployed by NOAA's HMT program at Alta (ATA, 1085 m MSL) and Colfax (CFC, 636 m MSL) over the Sierra Nevada, and Cazadero (CZC, 475 m MSL) near the coast (see Fig. 1c for the locations). The stationary vertically pointing antenna enables profilers to study the vertical structure of precipitation systems as they pass over the radar site [*Gage et al.*, 2002]. In order for the S-PROF radars to observe both high altitude anvil clouds and low altitude heavy precipitation, the S-PROF radars sequence through three operating modes [*White et al.*, 2000]. Over a 2-minute window, the radar dynamic range changes to observe heavy precipitation (30-sec), moderate precipitation (30-sec), and then anvil clouds (60-sec). The S-PROF radars are used primarily for real-time HMT applications by analyzing the vertical gradient in Doppler velocity to identify the height where frozen particles are melting into raindrops [*Williams et al.*, 1995; *White et al.*, 2002]. The S-PROF radar observations are not routinely calibrated to produce reflectivity estimates. Therefore, this study followed the procedure outlined in *Williams et al.* [2005] to cross-calibrate the three modes and absolutely calibrate against a surface Parsivel disdrometer. Before merging the three modes into a calibrated data set with a 1-minute time and 60-m vertical resolution as used in this study, outliers for each mode were removed by eliminating observations near the levels of detectability and saturation (i.e., levels of low and high signal-to-noise ratio).

[18] Figure 1 shows the observations by the AMSR-E high-frequency channels at 89 GHz. The warm brightness temperatures over the eastern Pacific correspond to the atmospheric river, where radiance emission from water vapor contributes to the warm T_b detected by the sensor (Fig. 1a). The colder PCT89 ($< \sim 260$ K) values shown in Figs. 1b and c depict the scattering signature associated with the precipitation structure and suggest that precipitation formed as the AR approached the coastal region. The banded cold PCT features perpendicular to the California coastline correspond to rainbands that were parallel to the cold front and the AR. Cold PCT values over the Sierra Nevada (with the minimum value of ~218 K) indicates the occurrence of precipitation enhanced by strong orographic forcing.

[19] The vertical structure of the precipitation system, including radar reflectivity and Doppler velocity, is shown in Fig. 2 as the system passed over the three S-PROF sites. Precipitation began at the sites on 30 December (not shown) as the AR moved onshore and over the mountains ahead of the surface cold front (arrows in Fig. 2 show the time of the frontal passage, as indicated by a sharp decrease in surface temperature field.). This event was characterized mainly by pre-frontal stratiform precipitation. The precipitation was moderate (35–40 dBZ) most of the time, with one or two intense ($>$ 40 dBZ) periods that lasted a couple of hours at the individual sites. This localized intensification was likely due to interactions between the intense baroclinic zone and the rough terrain of the mountains and valleys. The radar brightband was very prominent at these sites with the highest reflectivity (sometimes exceeding 50 dBZ) occurring at ~ 2.5–2.75 km MSL. Above the melting layer, the reflectivity in the snow layer was relatively weak ($<$ 30 dBZ). The time-height cross sections of Doppler velocity at the three S-PROF sites (Fig. 2b, d, and f) readily distinguish

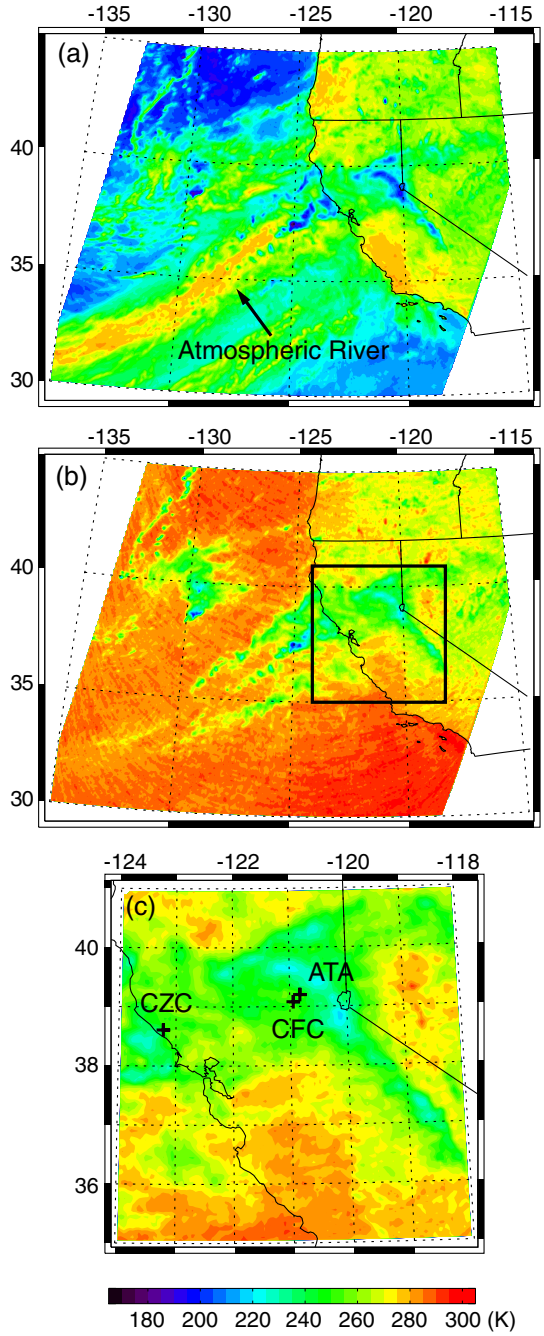

Figure 1. AMSR-E 89 GHz (a) brightness temperature from the horizontal polarization channel and (b, c) Polarization Corrected Temperature (PCT) at 10:16 UTC 31 December 2005. (c) is a zoomed-in view of the area inside the box of (b), which corresponds to the innermost domain in model simulations. Cross signs denote the locations of the S-PROF radars.

the layers of snow and rain. The magnitude of the Doppler velocity was 5–10 m s^{-1} in the rain layer and less than 2–3 m s^{-1} in the snow layer.

[20] Figure 3 summarizes the S-PROF observations with a 2-D histogram that shows the distributions of the reflectivity and Doppler velocity magnitudes with respect to height. Consistent with the time-height plots (Fig. 2), a prominent

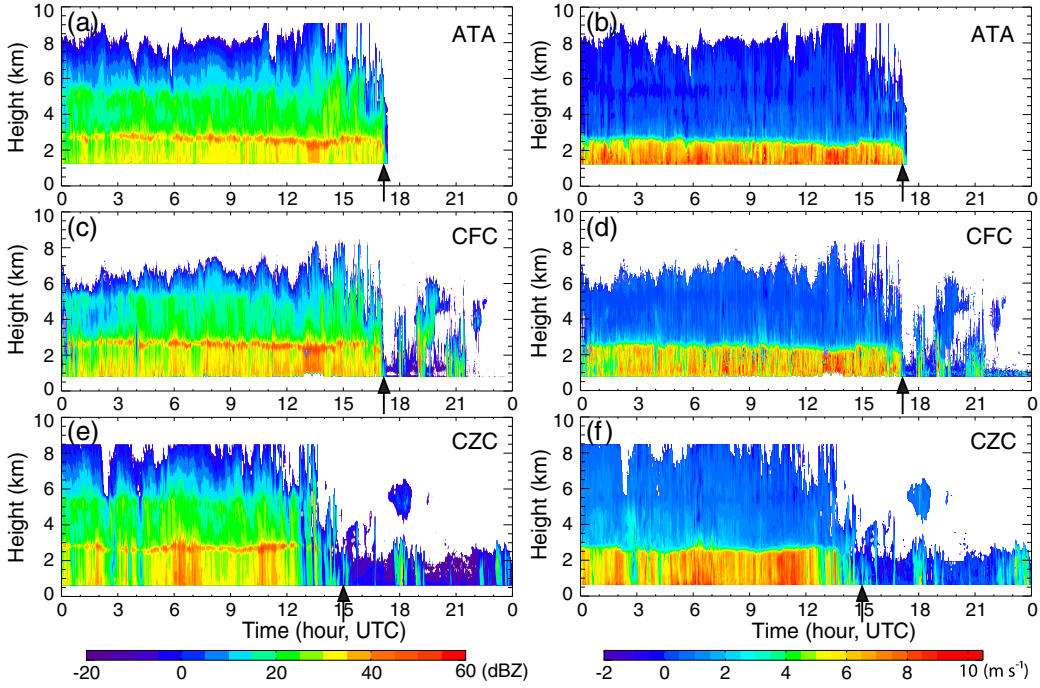

Figure 2. Time-height (MSL) cross sections of (a, c, e) radar reflectivity (dBZ) and (b, d, f) Doppler velocity ($m\,s^{-1}$) observed by S-PROF on 31 December 2005. Positive values in the velocity panels mean downward motion. The arrows show the time when the cold front passed the site, as indicated by a sharp decrease in surface temperature field.

thin layer of large reflectivity occurred at ~2.5–2.75 km MSL in association with the radar brightband (See Figs. 3a, c, and e). A secondary maxima in reflectivity is apparent at ~ 5 km MSL within the ice layer, and likely was related to turbulence in the vicinity of topography that enhanced the growth of snow aggregates. [e.g., *Houze and Medina*, 2005]. The Doppler velocity histograms (Figs. 3b, d, and f) show the distinct contrast in the magnitudes of the velocities in the snow and rain layers, with a gradual increase of speed in the transition zone. The CZC Doppler velocity 2D histogram shows a distribution near zero velocity up to about 2 km that was due to the S-band radar's detection of shallow light rainfall or drizzle along the coast after passage of the front.

4. Model Simulations

[21] The four model simulations produced similar dynamic and thermodynamic environments that have been validated against reanalysis data provided in *Smith et al.* [2010] for the same case. The simulated ambient conditions, including moisture and stability, was also verified with soundings at Oakland, CA and Reno, NV. The simulations captured a fairly consistent structure and strength of the AR as indicated by integrated water vapor and surface wind fields. The above verification procedure for this study is not included in this paper due to space limitations. However, differences on the timing of front passage at each station will be briefly noted when simulated reflectivity is analyzed in Section 4c.

a. Vertical profile of hydrometeors

[22] The four simulations with different microphysics schemes produce large differences in hydrometeor profiles. Figure 4 compares the vertical profiles of 5 hydrometeor species that were averaged within a region over the Sierra Nevada mountains (shown in Fig. 5 by the black outline). The profiles of rain are similar among the four schemes except that the THOM run produces ~20% less rain than the other runs. The GSFC run results in slightly more snow than the THOM and MORR runs and produces a moderate amount of graupel. The WSM6 run produces the largest amount of graupel and much less snow than other schemes. The snow profiles in THOM and MORR are similar, particularly below 6 km. THOM has somewhat more snow than MORR above 6 km, where THOM shows nearly no cloud ice (Cloud ice in THOM is categorized as very small snow particles). MORR has a moderate amount of graupel, while THOM has the least amount of graupel.

[23] Cloud water extends to very high altitudes (9 km) in the WSM6, THOM, and MORR runs, while it only reaches 6 km in the GSFC run. The cloud ice profiles in GSFC, WSM6 and MORR show notable differences, particularly in terms of the heights of the base of this layer and the level of maximum cloud ice. Since the observations used in this study are mainly sensitive to precipitation-sized hydrometeors, only the differences in the profiles of the precipitation species will be discussed further in the following sections.

b. Simulated PCT

[24] The simulated PCTs at 89 GHz (Fig. 5) from each scheme qualitatively capture the precipitation signature over the Sierra Nevada range and the coast. The magnitudes of the simulated PCTs are 20 K or more lower than the observed values (see Fig. 1c), indicating that the scattering

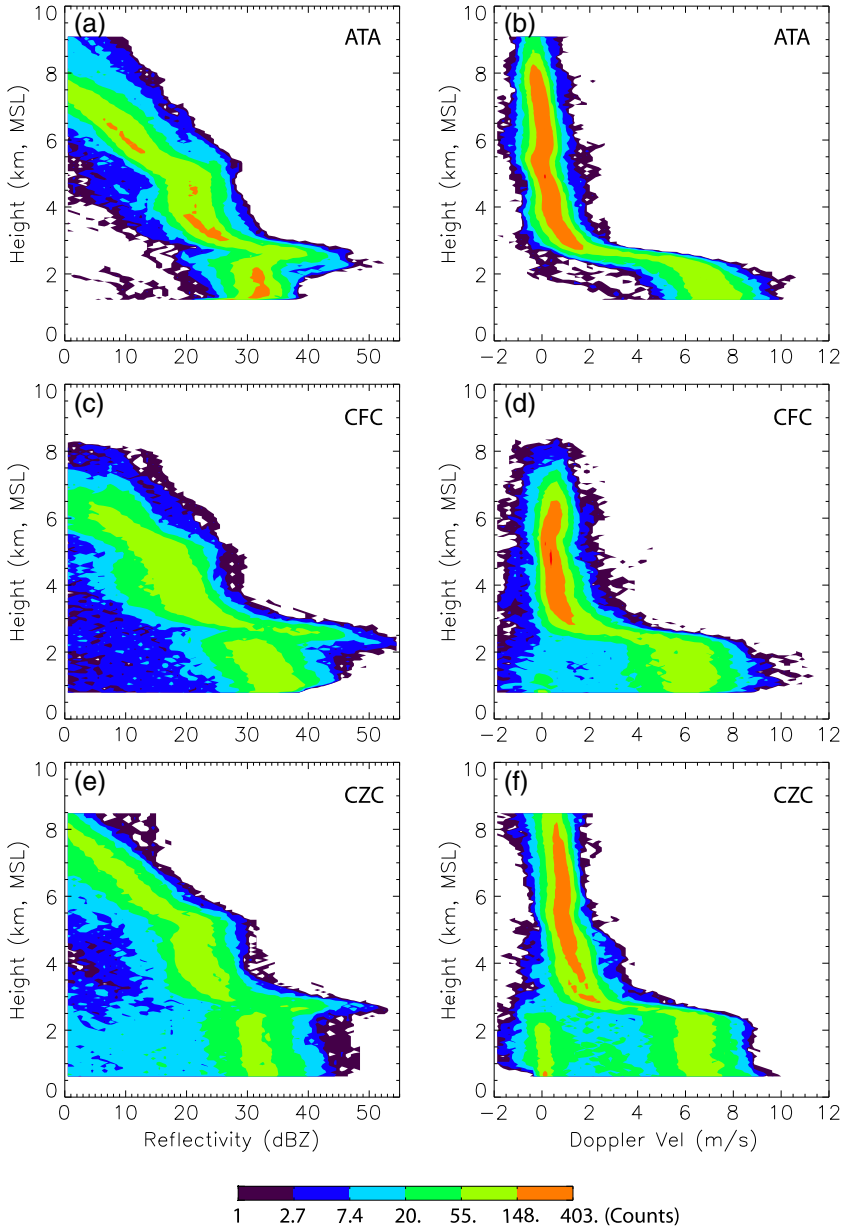

Figure 3. Two-dimensional histograms of observed reflectivity (dBZ) and Doppler velocity ($m\,s^{-1}$) as a function of height at ATA, CFC, CZC, on 31 December 2005.

signals are generally too strong in the simulations. The scattering is particularly strong over the Sierras. The area with moderate scattering (green shaded, corresponds to the existence of precipitation hydrometeors) is more wide-spread than in the observations. The precipitation structure near and to the north of 40° N show very low PCT values in the simulations, which do not agree with the observations and are not discussed in this study. The MORR run (Fig. 5d) predicts somewhat less scattering over the Sierras and appears to be in better agreement with the observations in that region than other schemes. However, its scattering signature in the coastal region, north of San Francisco, is stronger than the others. As noted in section 2b, T_b and PCT calculations for THOM uses prognostic variables from the WRF run, but PSD information required for the radiative transfer calculations utilizes the GSFC PSD assumptions. Therefore, Fig. 5c only gives an estimate of the scattering signature that is produced with the THOM scheme. As such, it also shows scattering that is too strong over the Sierras.

[25] In order to further investigate the individual contributions to the scattering signature by snow and graupel, a partitioned PCT89 was calculated for the GSFC, WSM6, and MORR simulations (Fig. 6). In this calculation, only one type of hydrometeor species (e.g., snow or graupel) and water vapor are included. For the GSFC and MORR schemes, snow contributes more to the precipitation scattering signature than graupel, which is consistent with the dominant mass of snow as shown in Figs. 4a and 4d. In contrast, scattering in the WSM6 run is dominated by graupel since, for the same amount of mass, graupel is a more efficient scatterer because of its higher effective density.

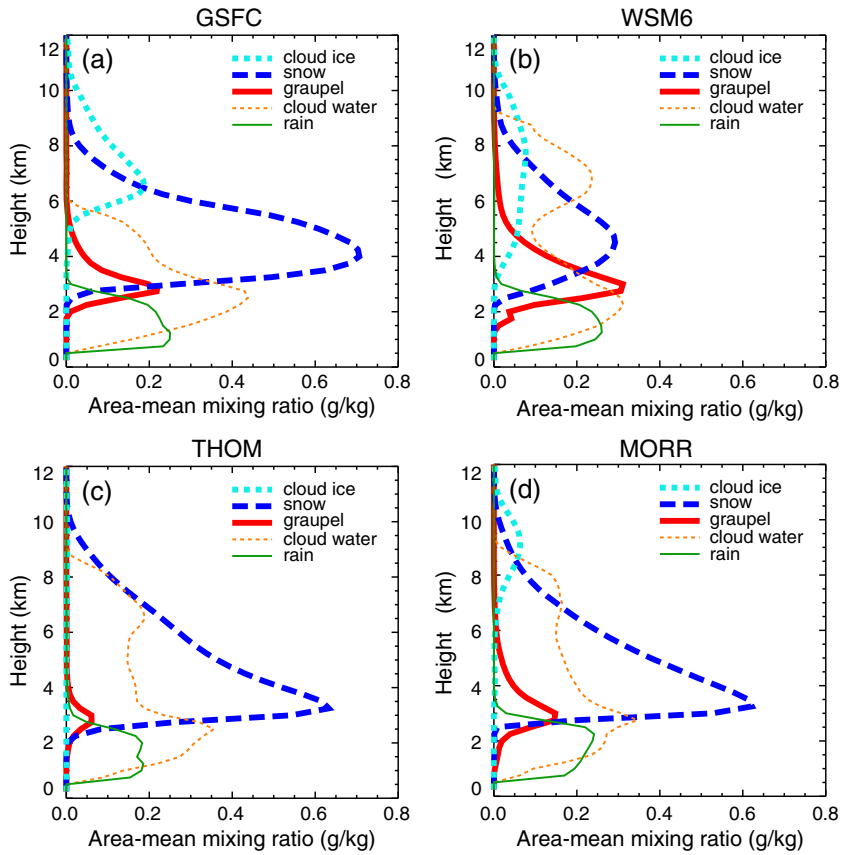

Figure 4. Area-mean profiles of hydrometeor mixing ratios for five cloud and precipitation species from the four microphysics schemes at 10 UTC 31 December 2005. Figure 5 shows the location of the averaging area (enclosed by the black outline) that is over the Sierra Nevada range with terrain height above 500 m and to the south of 40° N.

[26] The overestimate of ice scattering in microwave T_b has been reported in other studies using bulk microphysics [e.g., *Matsui et al.*, 2009; *Han et al.*, 2010] and even spectral-bin microphysics [*Li et al.*, 2010], and is believed to be caused by overestimation of the precipitation ice mass (snow or graupel) and/or inaccurate particle sizes represented in the cloud microphysics schemes. In this study, we found that this bias is common among the four schemes. The change of scattering intensity as a function of particle size is non-monotonic. In order to improve model simulations of precipitation ice scattering, further study will be needed to evaluate and improve the simulated total mass of precipitation ice, the partitioning between snow and graupel, and the size distributions of the precipitation particles.

[27] Utilizing the GSFC PSD assumptions to calculate T_b in the THOM run leads to inaccuracy. The sizes of precipitation particles used in the G-SDSU for THOM do not agree with the particle sizes represented in the WRF simulation. Han et al. [2010, their Fig. 12] suggest that the size of precipitation particle plays a secondary role when determining the scattering properties of ice in an atmospheric column, while the total mass of the hydrometers plays a major role. Therefore, overestimates of scattering in THOM likely imply too much mass of precipitation ice, consistent with other schemes. However, future research may be necessary to investigate whether simulated scattering signatures could be improved if the particle sizes in the THOM scheme are well represented in the G-SDSU.

[28] It should be noted that the G-SDSU adopted a "soft-sphere" approximation for precipitation hydrometeors when calculating the single scattering properties with the Lorenz-Mie solution. This approximation causes low bias in simulating scattering intensity [*Liu*, 2004] due to reduced forward scattering. If a more accurate non-spherical single scattering database (e.g., through discrete-dipole approximation modeling) could be used, it is likely that an even greater bias (> 20 K) could have been produced in the simulated PCT89.

c. Simulated equivalent radar reflectivity factor

[29] Figure 7 shows the simulated equivalent radar reflectivity factor Z_e in dBZ units (in short, "radar reflectivity") from simulations with the GSFC, WSM6, THOM, and MORR schemes at the three S-PROF sites. The time-height cross sections have a 5-min temporal and a 0.25-km vertical resolution that was interpolated from the original vertical levels in the WRF simulations. The time when the front passes each site, determined from a time series of surface temperature fields, is indicated with triangles. The simulated frontal passage time occurs ~2-3 hours earlier than observed (see Fig. 2), except MORR shows a closer timing for the frontal passage. However, the time when the precipitation

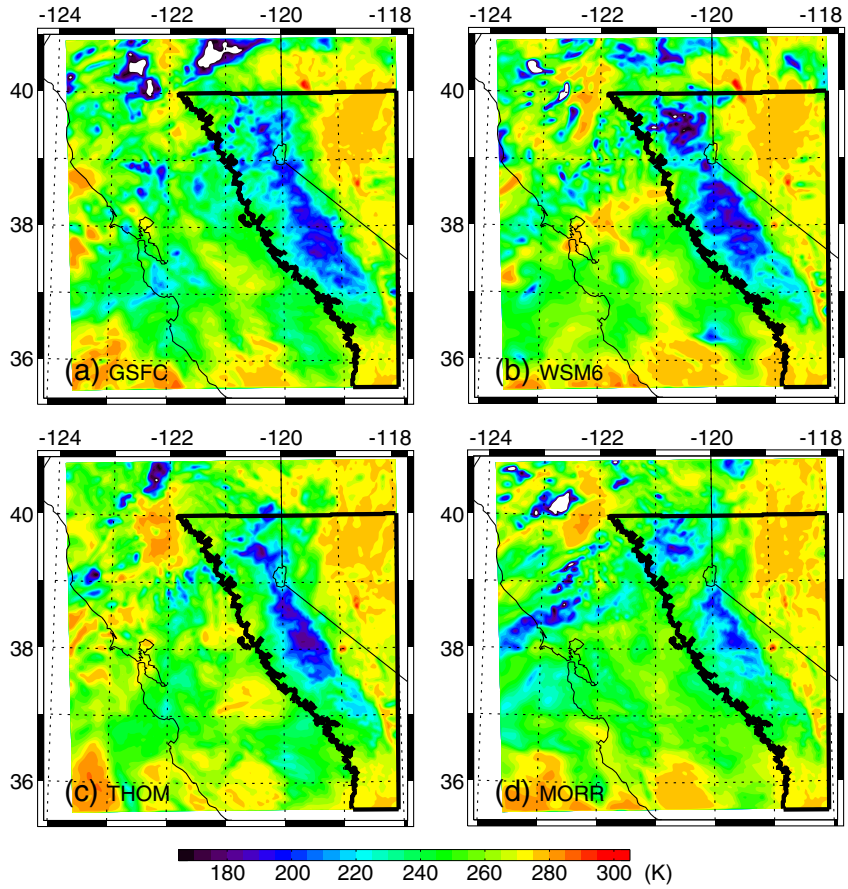

Figure 5. Simulated PCT89 (K) for the (a) GSFC, (b) WSM6, (c) THOM, and (d) MORR schemes at 10 UTC 31 December 2005. The area enclosed by the black outline is used to calculate the mean vertical profiles hydrometeors shown in Fig. 4.

ends at each site in the simulations agree well with that in the observations. Our analysis focuses on the magnitudes of reflectivity and Doppler velocity during the whole precipitating period on 31 December 2005.

[30] The simulated reflectivity magnitudes have large variations among the four simulations (Fig. 7). Since the simulated reflectivity calculation does not include the effect of melting on back-scattering cross section, a radar brightband is not produced in the simulations. However, the location of the freezing level at ~2.5 − 3 km MSL is still apparent. The rain layer generally has higher reflectivity values than above the freezing level in most simulations, with the exception of the MORR simulation that produces comparable reflectivities in both layers. The GSFC and WSM6 schemes (Figs. 7a−7f) produce similar reflectivities and both agree with the observations reasonably well in the rain layer when compared to the S-PROF measurements (Figs. 2a, c, and e). In contrast, the reflectivities above the freezing level are ~5 − 8 dBZ higher than observations. The THOM scheme produces much weaker reflectivities (< 30 dBZ) in the ice layer, which is in good agreement with the observed magnitudes. Its magnitude in the rain layer also agrees reasonably well with the observations. The simulation with the MORR scheme produces reflectivities that are too strong in both rain and ice layers, with ~5 dBZ higher values in the rain layer and ~10−12 dBZ higher values in the ice layer as compared to the observations.

[31] In Figure 8, the statistics of the simulated reflectivity at the three S-PROF sites are summarized within "combined" 2D histograms and compared to the observations (contours in Fig. 8 and Figs. 3a, c, and e). The histograms further illustrate differences between the simulated and observed magnitudes of radar reflectivity. Consistent with Fig. 7, Fig. 8 shows that the simulations generally lack prominent radar brightbands at ~2.5 km MSL and the secondary reflectivity maximum at ~5 km MSL. In terms of the modes shown in the histograms, GSFC, WSM6, and MORR show a high bias of ~5 − 10 dBZ in the ice layer above 3 km MSL. MORR also shows a large amount of points that exceeds ~40 dBZ above 3 km MSL. The reflectivity histogram with the THOM scheme agrees well with the observations in the rain and ice layers. Such contrasts in the simulated reflectivity magnitudes with the different schemes will be discussed in the next subsection.

d. Factors that influence the magnitude of the simulated reflectivity

[32] In order to understand the underlying causes of the high bias in the simulated reflectivities in the ice layer, the effective radius is analyzed. The effective radius, R_e, is defined as half the ratio of the third moment of the size

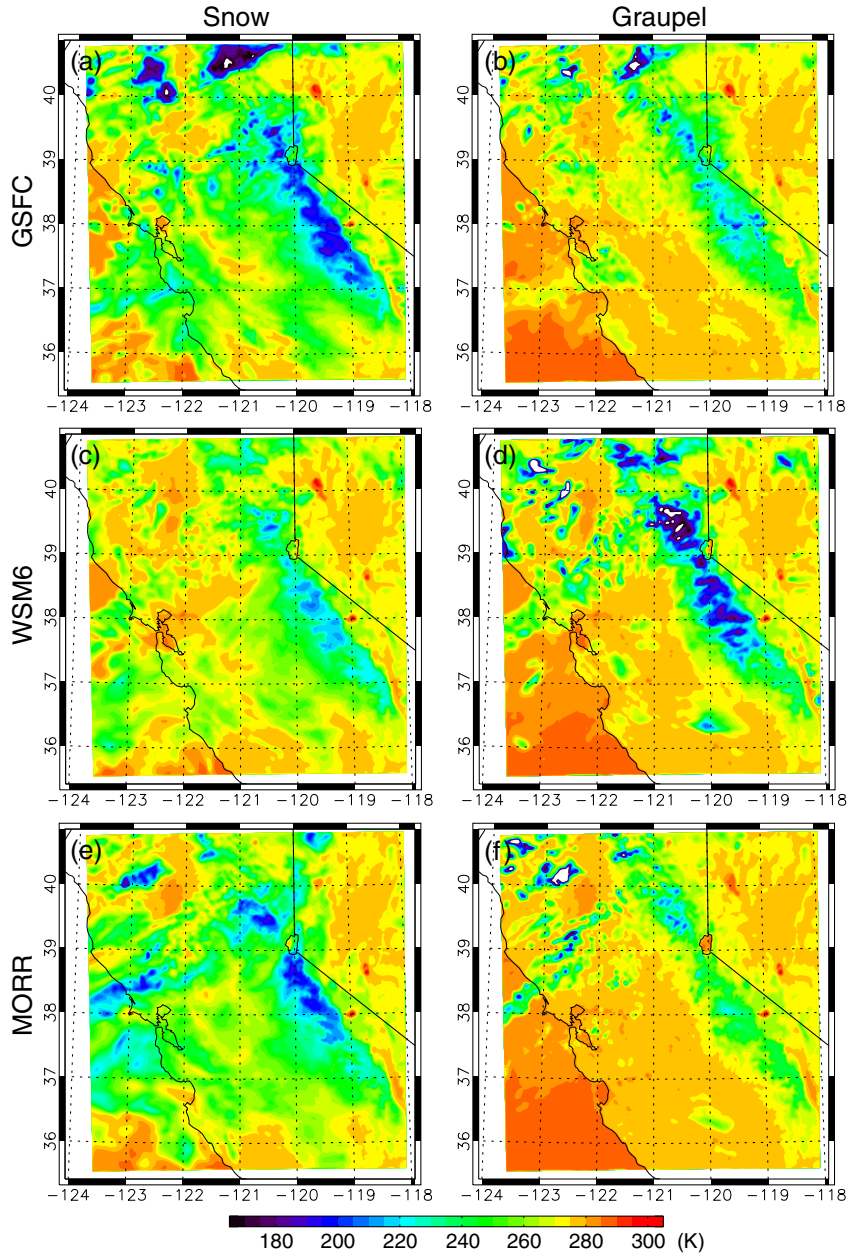

Figure 6. Partitioned PCT89 due to (a, c, e) snow and (b, d, f) graupel for (a, b) GSFC, (c, d) WSM6, and (e, f) MORR at 10 UTC 31 December 2005.

distribution of the precipitation particles to the second moment, following *McFarquhar and Heymsfield* [1996]:

$$R_e = \frac{D_e}{2} = \frac{\int N(D)D^3 dD}{2\int N(D)D^2 dD} \tag{11}$$

[33] For particles with a gamma size distribution and a zero value for the shape parameter (applicable to all the hydrometeor species in the four schemes except snow in THOM),

$$R_e = 1.5/\lambda, \tag{12}$$

where λ is the slope parameter in the distribution function (see Eqs. 1, 5, and 7). For snow in THOM, R_e is calculated directly from the ratio of its moments.

[34] Figure 9a shows histograms of the diagnosed snow R_e for the four simulations within their innermost domains at all vertical levels. The THOM scheme produces the largest number of small snow particles and the lowest number of larger particles. The MORR scheme produces a relatively large amount of small particles, a moderate amount of particles between 500 − 1500 μm and a small amount of large particles ($R_e \sim 2000$ μm). These large snow particles are collocated with areas of large reflectivity (> 40 dBZ) in the ice layer. The R_e histograms for GSFC and WSM6 are similar to MORR for $R_e < \sim 1500$ μm, but with fewer small particles. Thus the high biases in reflectivity in GSFC, WSM6, and MORR result from the large numbers of particles in the 500 − 1500 μm range, with additional bias in MORR coming from small numbers of very large

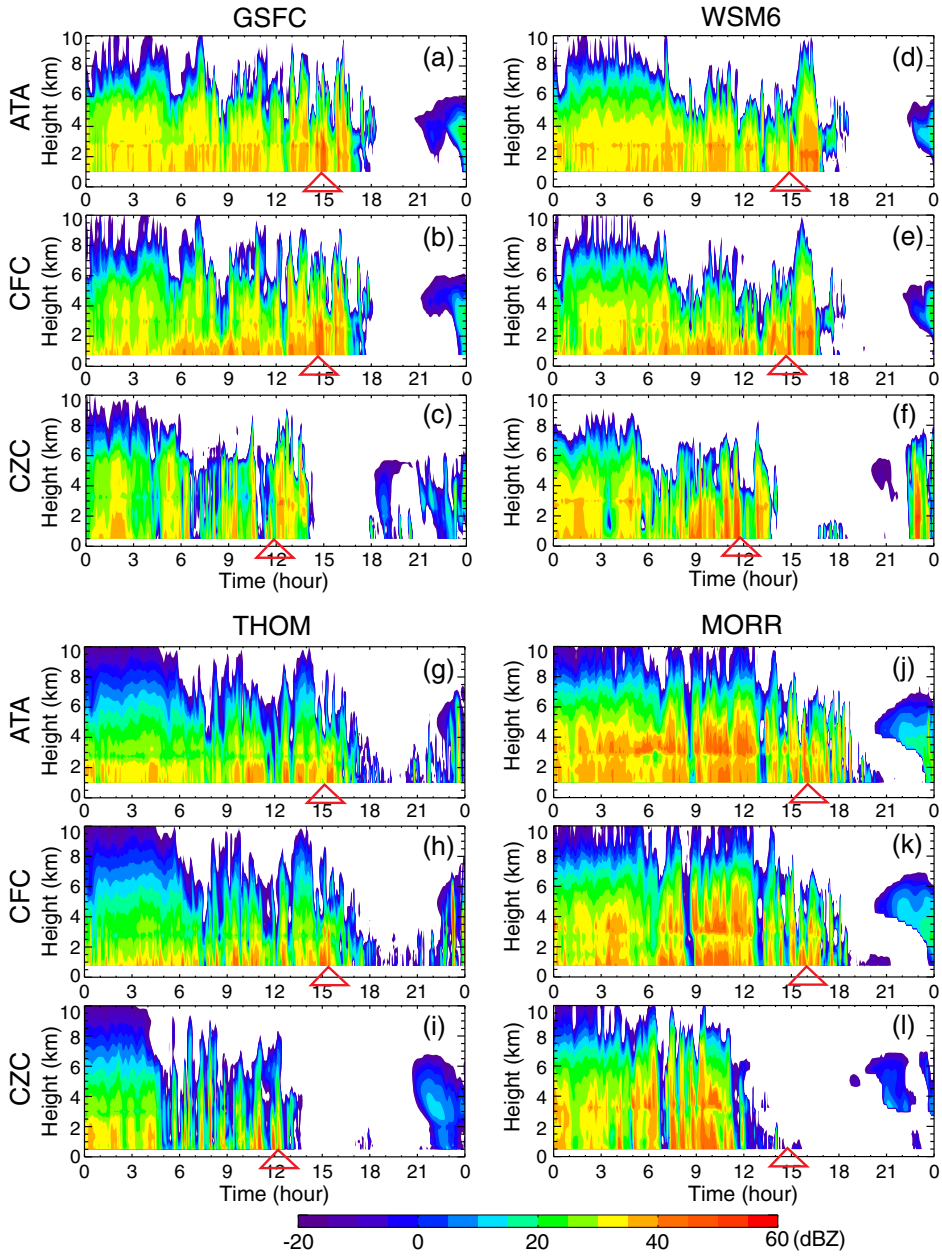

Figure 7. Simulated time-height (MSL) cross sections of radar reflectivity (dBZ) for the four microphysics schemes, (a, b, c) GSFC, (d, e, f) WSM6, (g, h, i) THOM, and (j, k, l) MORR and for the three S-PROF sites at ATA, CFC, and CZC on 31 December 2005. The triangles' top points show the time when the cold front passed the site, as indicated in simulated surface temperature field.

particles. Since bulk microphysics schemes do not directly calculate the size distribution of hydrometeor species, it remains to be determined how the PSD assumptions relate to the differences in R_e (Eq, 12).

[35] Recall that the slope parameter λ is diagnosed from the predicted mixing ratio, particle bulk density, and prescribed intercept parameter N_{0s} (for single-moment hydrometeor species, Eq. 5) or number concentration N_s (for double-moment hydrometeor species, Eq. 7). For a specified mixing ratio and bulk density, deviations in the prescribed intercept parameter or predicted number concentration from observations may result in errors when characterizing particle sizes (R_e) and simulating radar reflectivity. Indeed, *Han et al*. [2010], among a number of other studies [e.g., *Gilmore et al*. 2004; *Bryan and Morrison*, 2011], found that there is a strong dependence of the simulated reflectivity on the prescribed intercept parameters in five different schemes in the MM5 model. *Han et al*. [2010] also suggested that the best estimate for N_{0s} is on the order of 10^8 m^{-4} for a frontal precipitation system, which is consistent with the value of ice PSDs found in an in-situ observational study of tropical stratiform clouds [*Tian et al*., 2010]. When the value of N_{0s} decreases from 10^8 to 10^7 m^{-4}, the reflectivity increases ~4−5 dBZ because the sizes of the particles increase. Thus one of the possible causes for the high bias of reflectivity in the ice layer in the GSFC scheme might be its N_{0s} value

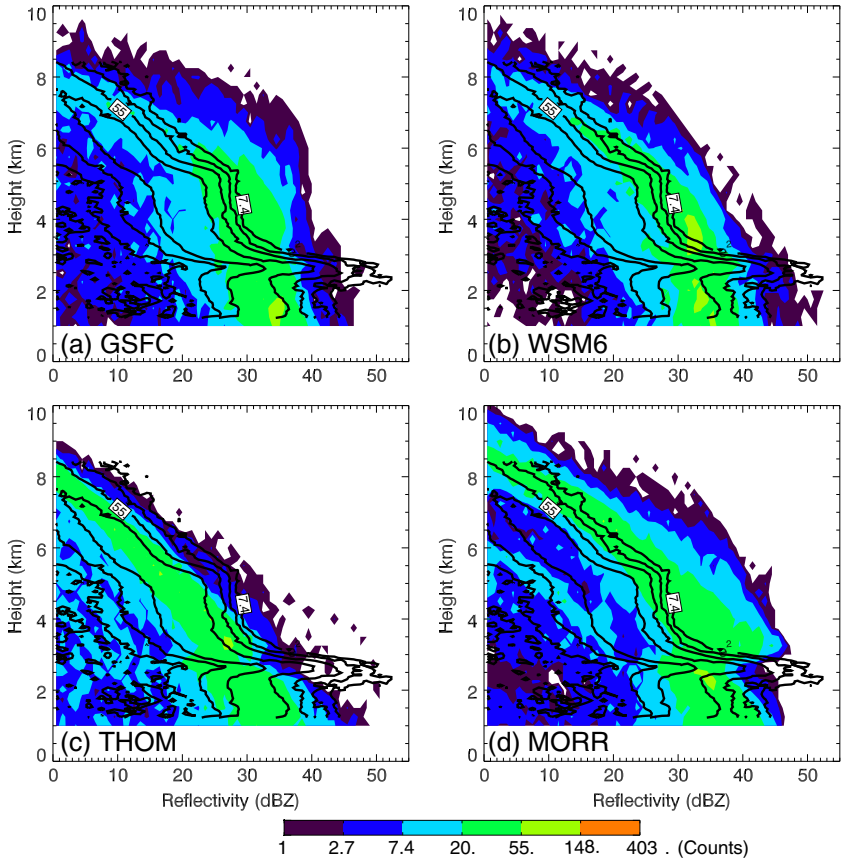

Figure 8. Combined two-dimensional histograms of simulated (shaded, for four schemes) and observed (contours) reflectivity (dBZ) as a function of height on 31 December 2005. The combined histograms include data from all three S-PROF sites. For example, contours for the observations represent the sum of the histograms in Figs. 3a, c, and e. The contour levels are 7.4, 20., 55., and 148.

(Table 1) being one order of magnitude smaller than expected values for this type of precipitation system. Similarly, in the WSM6 scheme, where N_{0s} increases with decreasing air temperature, the values of N_{0s} are less than 1×10^7 m^{-4} below 6 km MSL and less than 1×10^8 m^{-4} below 8 km MSL. Their values also appear to be too small and may contribute to the high bias in reflectivity simulation above the freezing level.

[36] The good reproduction of the reflectivity distribution with the THOM scheme might be tied to its unique snow PSD assumptions that leads to smaller particle sizes as shown in Fig. 9a. It is important that its *m-D* relationship resulting from the fractal-like assumption of snow aggregates contributes to a better characterization of the backscatter cross section of snow than the *m-D* relationship for spheres assumed in other bulk microphysics schemes. These assumptions might be particularly representative for wintertime precipitation systems since the snow PSD in the THOM scheme was constrained by in-situ measurements obtained under synoptic environments similar to the current study [*Field et al*., 2005].

[37] Given the relationship between R_e, λ, N_0, and N (Eqs. 5–7, and 12), we investigate why the MORR scheme produces much larger reflectivity peaks than the other schemes. The scatter plot of q_s *vs.* N_s for grid points with $2000 < R_{es} < 3000$ μm for snow at ATA in MORR is shown in Fig. 9b. It demonstrates that these points are associated with $N_s < 2000$ m^{-3} and a reasonable range of snow mixing ratio consistent with other three schemes. For a given snow mixing ratio, if the snow number concentration is too small, it could lead to large snow particle sizes that then contribute to unrealistically large reflectivities. To illustrate this point, we compare the value of N_s in the MORR scheme with estimated N_s from other schemes with specified N_{0s} based on Eq. 6. In Eq. 5, the value for N_{0s} is chosen to be 1×10^7 or 1×10^6 m^{-4} and the snow water content ($\rho_a q_s$) is specified to range from 0.2 to 2 g m^{-3}. Calculations (Eqs. 6 and 12) yield the relationship between N_s and R_{es} for a given magnitude of N_{0s} and snow water content (Fig. 9c). First, for $N_{0s} = 1\times10^7$ m^{-4}, which represents the magnitude of N_{0s} for the GSFC scheme, Fig. 9c indicates R_{es} between 700 to 1400 μm and N_s between 5000 and 9000 m^{-3}. Apparently, the estimated N_s value used in the GSFC scheme is ~2.5 to 5 times larger than the N_s values associated with the large reflectivities in the MORR simulation (Fig. 9b). Calculations with $N_{0s} = 1\times10^6$ m^{-4} yield values of R_{es} and N_s that are similar to those points with very large reflectivity values in the MORR simulation. This very small magnitude of N_{0s} suggests that the corresponding N_s values are very low and might be unrealistic.

[38] In summary, the above simplified calculations provide a means to compare the double-moment MORR scheme to the single-moment GSFC scheme. The results suggest that the low number concentration predicted in the

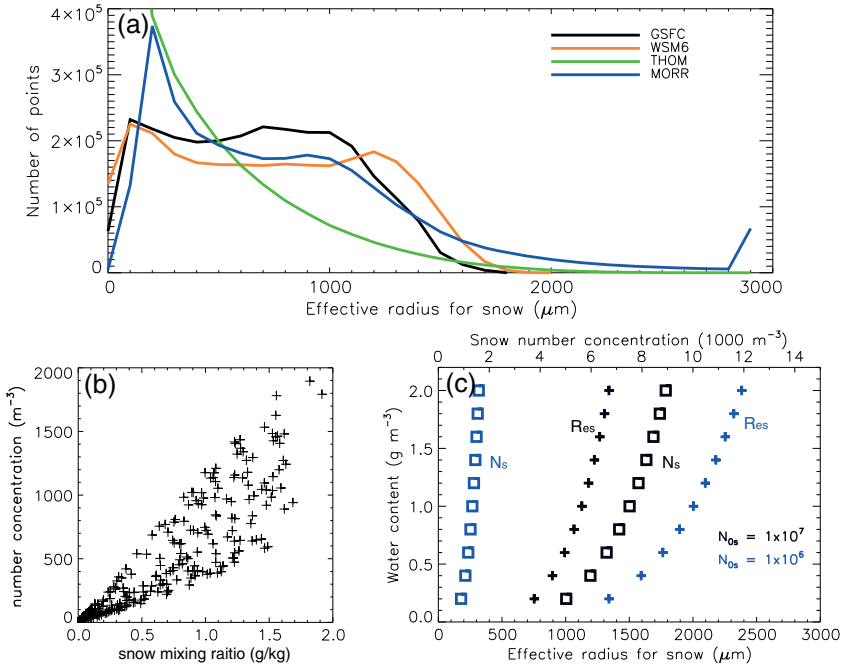

Figure 9. (a) Histograms of snow effective radius for the four schemes. Calculations are made over the entire innermost domain of the simulations. The spike feature near 3000 μm for the MORR scheme can be ignored in the analysis since it corresponds to points with near-zero mixing ratios. (b) Scatter plot of snow mixing ratio *vs*. number concentration for points with $2000 < R_{es} < 3000$ μm in the time-height plot at ATA for MORR scheme. (c) Idealized calculation of effective radius for snow (R_{es}, crosses), and snow number concentration (N_s, squares), for water contents ranging from 0.2 to 2 g m^{-3} with an interval of 0.2 g m^{-3}. The black lines are for $N_{0s} = 1 \times 10^7$ m^{-4} and the blue lines are for $N_{0s} = 1 \times 10^6$ m^{-4}.

MORR scheme is likely the cause for the excessive simulated reflectivity values. Similar findings of low bias in the number concentration from the double-moment scheme have been reported by *Solomon et al*. [2009] in an investigation of the microphysics of arctic clouds, where the number concentration in the MORR (WRF V2.2) double-moment scheme was ~ 1 L^{-1}, about 1 order of magnitude less than the observed value (see their Fig. 13).

[39] In addition to the contribution of the underestimated number concentration or intercept parameter to the high bias in reflectivity, particle densities can also be an important factor (see Eq. A.7). Observational studies [e.g., *Heymsfield et al*., 2004] have demonstrated that snow particle effective densities vary inversely with size. However, many bulk cloud microphysics schemes (including GSFC, WSM6, and MORR) still use a constant snow density. In contrast, a density-diameter relationship is indirectly adopted in the THOM scheme through its assumed *m-D* relationship [*Thompson et al*., 2008]. Their Fig. 1 shows that the density of snow is less than 100 kg m^{-3} (the value assumed in most microphysics schemes) when the particle diameter is larger than 1.2 mm. Given that a large portion of snow particles in the GSFC, WSM6, and MORR schemes (Fig. 9a) is larger than > 1.2 mm, it is inferred that the constant snow density used in these schemes may overestimate the densities of large particles and therefore also contribute to the high bias in simulated reflectivity.

e. Simulated Doppler velocity

[40] Since the particle fall speed is an important component in the simulated Doppler velocity, we first illustrate the relationship between the fall speed, $v_x(D)$, and diameter, D, for individual particles based on Eq. 10 and Table 2 at the reference vertical level (i.e., without considering the density adjustment factor) for the four schemes (Fig. 10). The parameters a and b in Eq. 10 were adopted by the individual schemes from earlier modeling and observational work [e.g., *Locatelli and Hobbs*, 1974; *Lin et al*., 1983; *Rutledge and Hobbs*, 1983; *Ferrier*, 1994]. GSFC, WSM6 and MORR use almost identical values of a and b for rain (all three schemes are indicated by the bold black circles in Fig. 10). The value of v_x for rain in THOM (green circles) is close to the other schemes when the particle diameter $D < 3.5$ mm, but much smaller at larger diameters. The v_x-D relationship for rain in *Atlas et al*. [1973] is indicated by the black curve for reference. For snow, fall speeds are smallest in the GSFC scheme, but similar among other schemes. Graupel particles in the GSFC and MORR schemes generally fall slower than those in WSM6 when their sizes are greater than 2 mm. Small graupel particles in THOM fall the slowest, while larger particles in THOM and WSM6 fall faster than those in GSFC and MORR.

[41] Time-height cross sections of the simulated Doppler velocities (Eqs. 8 and B.1 or B.2) at each S-PROF site for the four schemes are shown in Fig. 11 (see Figs. 2b, d, and f for the observations). Figure 12 shows the 2D histogram

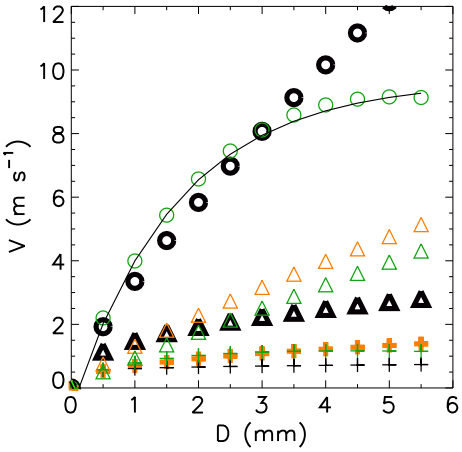

Figure 10. Relationship of particle fall speed, $v_x(D)$, and diameter, D, at reference level used in the four schemes (scattered shapes). Circles are for rain (Black is for GSFC, WSM6, and MORR, and green is for THOM.). Triangles are for graupel (Black is for GSFC and MORR, green is for THOM, and orange is for WSM6.). Crosses are for snow (Black is for GSFC, green is for THOM, and orange is for WSM6 and MORR.). The bold signs denote the v_x-D relationship applicable for more than one scheme. The black curve shows a v_x-D relationship for rain in *Atlas et al.* [1973], where $v(D) = 9.65 - 10.3\ exp(-0.6\ D)$, D is in mm, and $v(D)$ is in m s^{-1}.

for each scheme and the comparison to the observed histogram (see the overlaid contours and Figs. 3b, d, and f). First we compare the simulated and observed velocities in the layer above freezing level. For the GSFC scheme, the Doppler velocities agree well with the observations. The other schemes, however, show a high bias compared to the observed velocities. WSM6 appears to have Doppler velocities about 1 m s^{-1} faster from 3 to 8 km in altitude. This result is consistent with the snow and graupel particle fall speeds shown in Fig. 10, which are largest for this scheme. The larger amount of graupel mass (Fig. 4) in WSM6 is also a contributor to this high bias. Doppler velocities in THOM and MORR are generally larger than those in the GSFC scheme and observed by ~0.5−1 m s^{-1} above ~4 km MSL, consistent with their faster fall speeds for snow. It should be noted that due to difficulties in implementing into post-processing software, the simulation of Doppler velocity for the THOM scheme does not consider the modification of the snow fall velocity associated with the snow particles' riming factor, which is included in the WRF model. If the riming effect were accounted for, its Doppler velocity would be even larger.

[42] The simulated Doppler velocity in the rain layer shows a relatively similar performance across the four schemes. It may be attributed to the fact that the raindrop fall speeds are very similar among the different schemes (see Fig. 10) in this case. However, their performance depends on location. Most of the schemes have a ~2−3 m s^{-1} low bias (MORR has a slightly smaller bias of 1−2 m s^{-1}) at ATA. In contrast, these schemes show a 1−2 m s^{-1} high bias at CFC. The simulated Doppler velocities in all the schemes are in better agreement with the observations at CZC than the other sites, but do not capture the shallow layer of near 0 m s^{-1} velocities that occur after frontal passage.

5. Conclusions and Discussion

[43] The impact of four cloud microphysics schemes (GSFC, WSM6, THOM, and MORR) in the WRF model on the structure of a wintertime orographic precipitation system is analyzed and evaluated against remote sensing data obtained by a satellite radiometer and ground-based S-band radars. The hydrometeors' PSD and bulk density assumptions in the GSFC, WSM6, and MORR schemes in the WRF model are incorporated into the Goddard-Satellite Data Simulation Unit (G-SDSU). This ensures that the forward radiative calculations of brightness temperature are consistent with the microphysical assumptions in the NWP model. Furthermore, in order to compare the simulations to observations from the S-band vertical profiling radars, we have developed customized calculations of radar reflectivity and Doppler velocity for the different microphysics schemes under the Rayleigh approximation. The schemes range from single-moment to double-moment, and from simple exponential PSDs to a more complicated hybrid of exponential and gamma distributions. The formulas for reflectivity and reflectivity-weighted terminal velocity are applicable to different assumptions about spherical or arbitrary-shaped particles and different v_x-D relationship, as assumed in the individual schemes. Such customized calculations enable us to evaluate the performance of the different microphysics schemes and find possible areas for model improvement.

[44] Frontal passage at individual sites occurs a couple of hours earlier in several simulations than in the observations. This error likely does not contribute to the biases discovered in the simulated brightness temperature, radar reflectivity, and Doppler velocity, because most of the precipitation occurs ahead of the front and our analyses focus on the overall statistical characteristics of the precipitation fields.

[45] Simulations with the four microphysics schemes show notable differences in the hydrometeor vertical profiles, including cloud ice, cloud water, snow, graupel and rain. The mass profiles for the frozen precipitation particles, snow and graupel, play an important role in simulating the precipitation scattering signature that is observed by the AMSR-E 89 GHz channel. Overall, all the simulations overestimate (by ~20 K) the ice scattering signature despite their differences in microphysics assumptions and the snow and graupel vertical profiles, suggesting that the simulations are over-predicting the precipitation ice mass. Although not implemented here, the ice scattering signals would be even larger if we had used a non-spherical single-scattering database in the G-SDSU. The partitioned contributions toward ice scattering from snow dominates that from graupel in the GSFC and MORR schemes, while graupel scattering is dominant in WSM6, consistent with their hydrometeor mass amounts and the fact that graupel is a more effective scattering media due to its greater density.

[46] The magnitudes of simulated reflectivities in the rain layer are close to the observed values, except that MORR shows higher values. The reflectivities in the ice layer have ~5−10 dBZ high biases in the simulations with the GSFC, WSM6 and MORR schemes. MORR also shows an excessive reflectivity peak that exceeds ~40 dBZ in the ice layer. The simulation with the THOM scheme produces the best agreement with the observed reflectivity magnitude, which we argue is mainly due to its unique PSD, shape, and

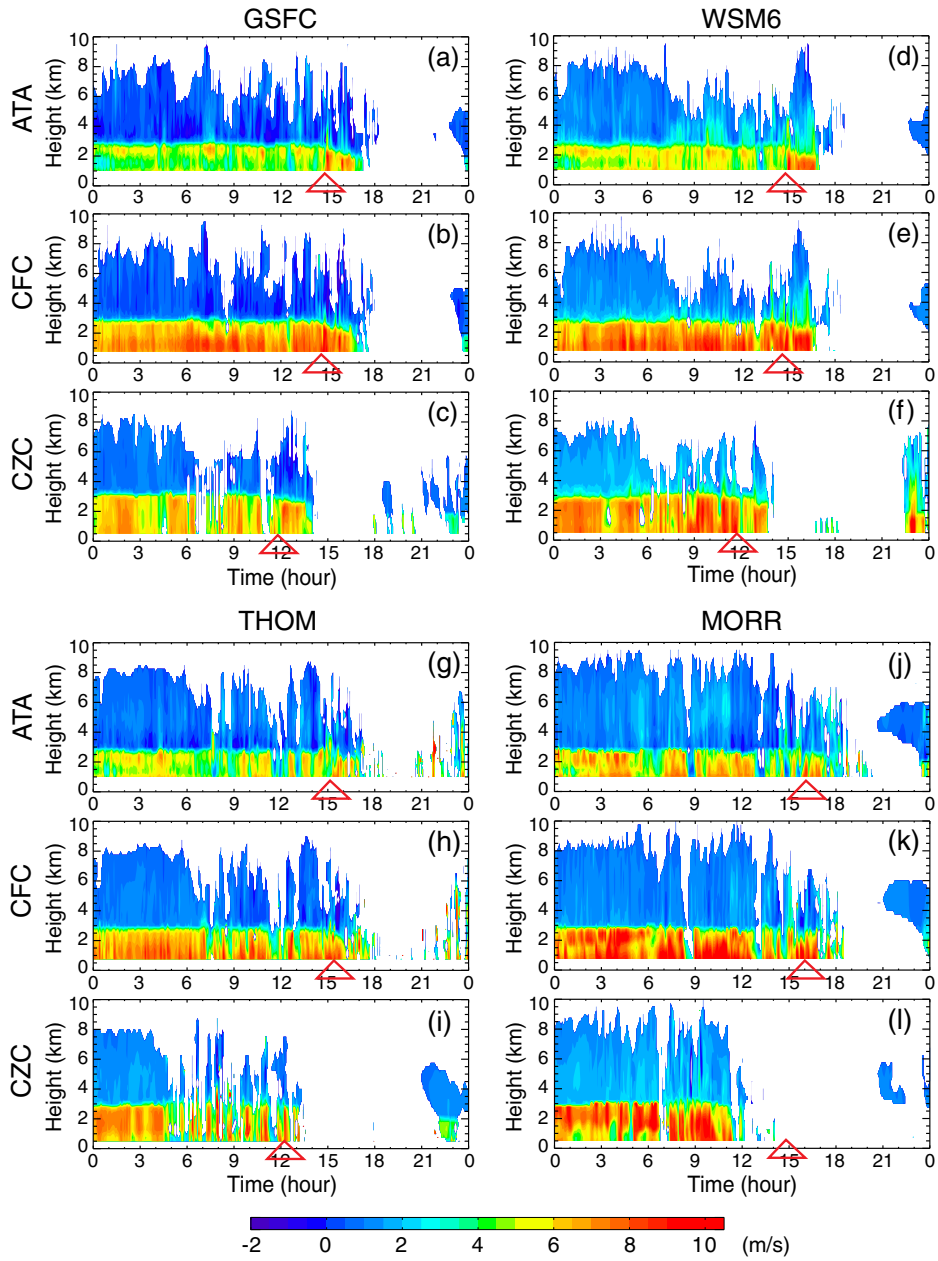

Figure 11. Same as Fig. 7, but for simulated Doppler velocity. Positive values mean downward motion.

density assumptions for snow species that result in a much smaller snow effective radius in this scheme than in other schemes. Given the assumptions related to snow particle shape in the GSFC, WSM6, and MORR schemes, the causes for the high bias in those schemes might be: 1) the relatively small intercept value N_{0s} (in the order of 10^7 m^{-4}) in GSFC and WSM6, which contributes to relatively larger snow particles, and 2) the low number concentrations and resultant large snow particle sizes in MORR. While it is difficult to find direct measurements of snow particle number concentrations for such frontal precipitation systems, our investigation suggests that the snow number concentration in MORR could be a factor of 2.5−5 smaller than that inferred from the GSFC scheme. Another factor that also contributes to the high bias in simulated reflectivities might be the assumption of constant snow density assumed in these three schemes.

[47] In this study, methods to calculate reflectivity are developed that are consistent with assumptions in each microphysics scheme. Assumptions about snow particle shape (*m-D* relationships) in the schemes determine whether the reflectivity is proportional to the 6th or the 4th moment of its PSD (see APPENDIX A). If the THOM *m-D* relationship were used in the reflectivity calculations for the GSFC, WSM6, and MORR schemes, it would act to make the reflectivity calculation dependent on the 4th moment, instead of the 6th moment, of the PSD, which would produce smaller reflectivity magnitudes that agree with observations better. Therefore, the snow *m-D* relationship assumption is a very important factor in reflectivity calculations. However, one cannot simply use an *m-D* relationship different from the scheme and infer impact on reflectivity. Because if that relationship was actually used in the scheme, it would affect

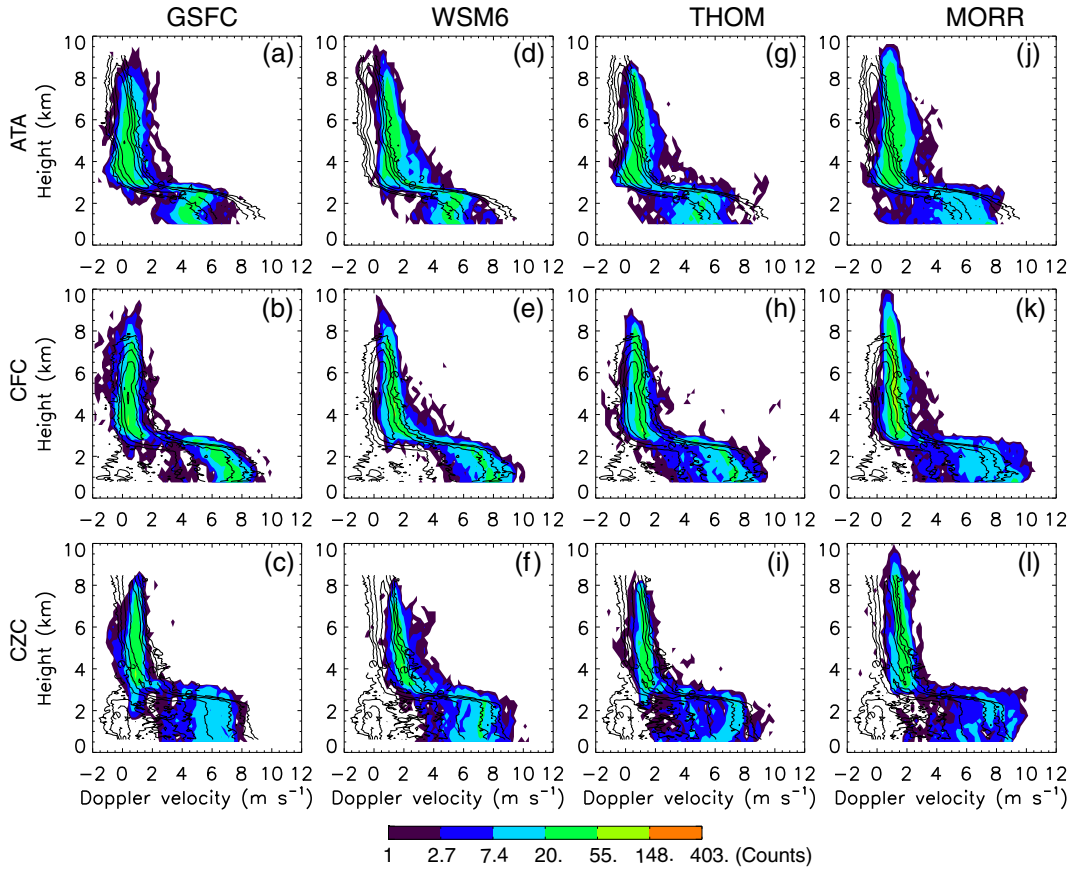

Figure 12. Two-dimensional histograms of simulated (shaded) and observed (contours) Doppler velocity ($m\,s^{-1}$) as a function of height at the three S-PROF sites (ATA, CFC, and CZC) and for the four microphysics schemes on 31 December 2005. The contour levels are 7.4, 20., 55.,148., and 403..

the collision kernels and terminal velocities etc., and the resultant mixing rations would be different. Further studies may be necessary to investigate if implementation of the THOM *m-D* relationship for snow in other microphysics schemes would result in improved reflectivity calculations in a physically consistent manner.

[48] It is beyond the scope of this study to investigate the causes of the small snow number concentration occurring in the MORR scheme, the only double-moment scheme in our study. The problem could be linked to an imbalance between the mass and number concentration as described in *Morrison et al*. [2005], resulting from errors occurring in the advection of a mixing ratio, q, and number concentration, N. Following suggestions in that paper, the current study employed a monotonic advection scheme available in WRF for moisture variables when using the MORR scheme. However, the low bias of N_s still occurs when q_s is in a reasonable range. Further research will be necessary to determine if the low values of N_s are caused by the numerical representation of the advection term, to test if such a problem is related to steep topography, and to improve the model representation of the number concentration. The small snow number concentration may also be linked to the way in which cloud condensation nuclei (CCN) and ice nuclei (IN) are initialized in the double-moment scheme, which determines cloud and ice number concentration and eventually the precipitation PSD. We used the default CCN and IN prescribed in the WRF model in this study. Sensitivity studies examining the CCN and IN initialization, with inputs from observed aerosol concentrations, might be necessary to further address this issue.

[49] The magnitudes of simulated Doppler velocity in the GSFC scheme shows good agreement with observations in the ice layer, while the other schemes have $\sim$1 $m\,s^{-1}$ high biases above 4−5 km MSL. The simulated Doppler velocity in the rain layer is similar among the four schemes, consistent with their v_x-*D* relationship assumptions for raindrops. The agreement between the simulated and the observed Doppler velocity in the rain layer varies with the location of the S-PROF site and may be related to effects of large topographic variability.

[50] The Doppler velocity obtained by the vertical profiling radar is the combination of vertical air motion and the terminal velocity of precipitation particles. It is difficult to estimate these components separately using instruments. This study is perhaps the first in attempting to simulate vertical Doppler velocity within precipitation systems using a NWP model with several different microphysics schemes. Such simulations provide a basis for evaluating the representation of particle fall speeds in the WRF modeling framework. It should be noted that the discrepancies between simulated and observed Doppler velocities found in

the rain layer need further investigation. Uncertainties in the characterization of vertical air motion and particle fall velocities at individual stations could be introduced by the high spatial variability of the terrain, its representation in the model, and the simulated flow response to this variability.

[51] Although the intercept parameter, N_{0s}, is found to be an important contributor to the high bias in the simulated reflectivity of the two single-moment schemes, GSFC and WSM6, modelers should not simply change the default value of N_{0s} in their simulations without validating the results with observations. Such changes may lead to improvement in one variable (e.g., radar reflectivity), but not necessarily in other variables (e.g., Doppler velocity or brightness temperature). In addition, the assumptions related to shape and density of precipitation ice particles are also important factors in calculating the radiative properties from the NWP model output. In other words, these radiative properties are not single valued functions. Methodologies should be sought to improve the model representation of cloud precipitation processes as a whole, not being limited to testing the sensitivity of just a few model parameters. Nevertheless, evaluating cloud microphysical schemes is a difficult task. Multi-instrument observations (remotely-sensed and in-situ) including satellite, aircraft, and ground-based data [e.g., *Molthan and Colle*, 2012; *Iguchi et al*., 2012], and accurate instrument simulators can provide better constraints to guide further development and improvement of cloud microphysical schemes.

[52] **ACKNOWLEDGEMENTS.** The author wants to thank Drs. Lin Tian, Liang Liao, Xiaowen Li, and Bill Olson at NASA/GSFC for many beneficial discussions related to radar algorithms and cloud modeling. Model simulations were performed on the NASS Discover Cluster. Comments from three anonymous reviewers were very helpful on improving the manuscript. This work was supported by Dr. Ramesh Kakar at NASA Headquarters with funds from the NASA Precipitation Measurement Mission science program.

APPENDIX A: Radar Reflectivity Calculations

[53] When simulating radar reflectivity from NWP models, the model-represented properties of hydrometeor particles need to be used to calculate the equivalent radar reflectivity factor (Z_e). Considering n categories of hydrometeor species, $Z_e = \sum_{x=1}^{n} Z_{ex}$, where $n = 3$ and x represents *snow*, *graupel*, and *rain* in the four microphysics schemes in the WRF model. The expression for individual hydrometeor category x is:

$$Z_{ex} = \frac{\lambda_{em}{}^4}{\pi^5 |K_l|^2}\eta_x = \frac{\lambda_{em}{}^4}{\pi^5 |K_l|^2}\int \sigma_x N_x(D)dD, \tag{A.1}$$

where λ_{em} is the wavelength of the electromagnetic wave transmitted from the radar and $|K_l|^2 = 0.92$ is the dielectric constant of liquid water. Because the size of precipitation particles is small compared to the wavelength of the S-band radar (10 cm), the Rayleigh approximation is valid for determining the back-scatter cross section [see *Battan*, 1973, pp 39]:

$$\sigma_x = \frac{36\pi^3}{\lambda_{em}{}^4}\frac{|K_x|^2}{\rho_x{}^2} m_x(D)^2, \tag{A.2}$$

where m_x and ρ_x are the mass and density of the hydrometeor particle, respectively, and K_x is the precipitation particles' dielectric coefficient. If particles are assumed to be spheres, $m_x(D) = \frac{\pi\rho_x}{6}D^3$, the backscattering cross section follows

$$\sigma_x = \frac{\pi^5}{\lambda_{em}{}^4}|K_x|^2 D^6 \tag{A.3}$$

[54] The value of the dielectric coefficient changes as the phase of particle changes. It can be estimated following Debye theory [*Battan*, 1973]: $\frac{K_x}{\rho_x} \approx \frac{K_{pi}}{\rho_{pi}}$, where $\rho_{pi} = 917.$ kg m^{-3} and $K_{pi} = 0.174$ are the density and dielectric coefficient of pure ice, respectively. By applying the Debye theory and substituting Eq. (A.2) into Eq. (A.1), we get the equivalent radar reflectivity factor, which is applicable to particles of arbitrary habit [also see Eq. 12 in *Hogan et al*., 2006]:

$$Z_{ex} = \frac{|K_{pi}|^2}{|K_l|^2}\left(\frac{6}{\rho_{pi}\pi}\right)^2 \int m_x(D)^2 N_x(D)dD \tag{A.4}$$

[55] For a hydrometeor species with assumed spherical shape, Z_{ex} is proportional to the 6th moment of the PSD,

$$\begin{aligned} Z_{ex} &= \frac{|K_{pi}|^2}{|K_l|^2}\frac{\rho_l{}^2}{\rho_{pi}{}^2}\frac{\rho_x{}^2}{\rho_l{}^2}\int D^6 N_x(D)dD \\ &= 0.224\frac{\rho_x{}^2}{\rho_l{}^2}\int D^6 N_x(D)dD, \end{aligned} \tag{A.5}$$

where $|K_{pi}|^2/|K_l|^2 = 0.174/0.92 = 0.189$ is the ratio of dielectric coefficients of pure ice and liquid water, and $\rho_l^2/\rho_{pi}^2 = 1000_2/917^2 = 1.189$ is the squared ratio of the densities of liquid water and pure ice.

[56] To account for the fractal-like, non-spherical shape of snow in the THOM scheme, substitution of Eqs. (3) and (4) into Eq. (A.4) yields a Z_{ex} that is proportional to the 4th moment of the PSD,

$$\begin{aligned} Z_{ex} &= \frac{|K_{pi}|^2}{|K_l|^2}\left(\frac{6c_x}{\pi\rho_{pi}}\right)^2 \int D^{2d_x} N_x(D)dD \\ &= \frac{|K_{pi}|^2}{|K_l|^2}\left(\frac{0.069\times 6}{\pi\rho_{pi}}\right)^2 \int D^4 N_x(D)dD = 3.91\times 10^{-9} M_4, \end{aligned} \tag{A.6}$$

where the forth moment M_4 is obtained following a rescaling procedure presented in Table 2 of *Field et al*. [2005]. For species with a gamma PSD and spherical-shape, substituting Eq. (1) into Eq. (A.5) gives

$$Z_{ex} = 0.224\frac{\rho_x{}^2}{\rho_l{}^2} N_{0x}\lambda_x{}^{-(7+\mu_x)}\Gamma(7+\mu_x), \tag{A.7}$$

where the slope parameter, λ_x, is diagnosed using the mixing ratio and/or number concentration (Eqs. 5 and 7). The intercept parameter, N_{0x}, is specified or diagnosed according to Table 1 and Eq. 6.

[57] The sum of the equivalent reflectivity factor from various categories of precipitation species, $Z_e = \sum_{x=1}^{n} Z_{ex}$, is in linear SI units, m^6 m^{-3}. It is usually converted to mm^6 m^{-3}, expressed in decibels (dB), and simply referred to as "radar reflectivity (dBZ)", i.e., $10 \times \log_{10}(10^{18} Z_e)$.

APPENDIX B: Reflectivity Weighted Terminal Velocity Calculations

[58] Similar to the reflectivity calculations, the derivation of reflectivity weighted terminal velocity (V_η, Eq. 9) for different microphysics schemes in the WRF model involves implementation of PSDs and fall speed-diameter relationships consistent with the assumptions in the WRF model. The formula for back scattering cross section (σ) under the Rayleigh approximation (A.2) or (A.3) is used in Eq. 9.

[59] For the WSM6, GSFC, and MORR schemes, substituting Eqs. 1, A.3, and 10 into Eq. 9 yields the formula for V_η:

$$V_\eta = \left(\frac{\rho_0}{\rho}\right)^{c_v} \frac{1}{720} \frac{N_{0r}|K_l|^2 a_r \lambda_r{}^{-(7+b_r)}\Gamma(7+b_r) + N_{0s}\frac{\rho_s{}^2}{\rho_{pi}{}^2}|K_{pi}|^2 a_s \lambda_s{}^{-(7+b_s)}\Gamma(7+b_s) + N_{0g}\frac{\rho_g{}^2}{\rho_{pi}{}^2}|K_{pi}|^2 a_g \lambda_g{}^{-(7+b_g)}\Gamma(7+b_g)}{N_{0r}|K_l|^2 \lambda_r{}^{-7} + N_{0s}\frac{\rho_s{}^2}{\rho_{pi}{}^2}|K_{pi}|^2 \lambda_s{}^{-7} + N_{0g}\frac{\rho_g{}^2}{\rho_{pi}{}^2}|K_{pi}|^2 \lambda_g{}^{-7}} \tag{B.1}$$

[60] Since the THOM scheme has a unique snow PSD and uses an exponential function in the particle v_x–D relationship, we derive a different formula for V_η by substituting Eqs. 1 and A.3 (for rain and graupel), Eqs. 2 and A.2 (for snow), and Eq. 10 into Eq. 9. It yields

$$V_\eta = \left(\frac{\rho_0}{\rho}\right)^{c_v} \frac{N_{0r}\pi^2|K_l|^2 a_r(\lambda_r + f_r)^{-(7+b_r)}\Gamma(7+b_r) + s1 + N_{0g}\pi^2\frac{\rho_g{}^2}{\rho_{pi}{}^2}|K_{pi}|^2 a_g \lambda^{-(7+b_g)}\Gamma(7+b_g)}{N_{0r}\pi^2|K_l|^2\lambda_r{}^{-7}\Gamma(7) + s2 + N_{0g}\pi^2\frac{\rho_g{}^2}{\rho_{pi}{}^2}|K_{pi}|^2\lambda_g{}^{-7}\Gamma(7)}, \tag{B.2}$$

$$s1 = coef \cdot a_s \left[\kappa_0 \left(\frac{\Lambda_0}{D_e} + f_s\right)^{-(5+b_s)} \Gamma(5+b_s) + \frac{\kappa_1}{D_e{}^{\mu_s}} \left(\frac{\Lambda_1}{D_e} + f_s\right)^{-(5+b_s+\mu_s)} \Gamma(5+b_s+\mu_s)\right], \tag{B.3}$$

$$s2 = coef \cdot \left[\kappa_0 \left(\frac{\Lambda_0}{D_e}\right)^{-5} \Gamma(5) + \frac{\kappa_1}{D_e{}^{\mu_s}} \left(\frac{\Lambda_1}{D_e}\right)^{-(5+\mu_s)} \Gamma(5+\mu_s)\right], \tag{B.4}$$

and

$$coef = 36 \times 0.069^2 \frac{M_2{}^4}{M_3{}^3} \frac{|K_{pi}|^2}{\rho_{pi}{}^2}. \tag{B.5}$$

[61] The term $D_e = \frac{M_3}{M_2}$ is the effective diameter [*McFarquhar and Heymsfield*, 1996].

References

Ashcroft, P., and F. J. Wentz (2006), updated daily, AMSR-E/Aqua L2A Global Swath Spatially-Resampled Brightness Temperatures V002, 12/31/2005. Boulder, Colorado USA: National Snow and Ice Data Center. Digital media.

Atlas, D., R. C. Srivastava, and R. S. Sekhon (1973), Doppler radar characteristics of precipitation at vertical incidence, *Rev. Geophys.*, *11*, 1–35.

Battan, L. J. (1973), Radar observation of the atmosphere, pp., 324, University of Chicago Press, Chicago, IL.

Blahak, U., Y. Zeng, and D. Epperlein (2011), Radar forward operator for data assimilation and model verification for the COSMO-model. *Preprint of 35th Conf. on Radar Meteorology*, Amer. Meteor. Soc., **P10.119**, Pittsburgh, PA.

Bryan, G. H., and H. Morrison (2011), Sensitivity of a simulated squall line to horizontal resolution and parameterization of microphysics, *Mon. Wea. Rev.*, *140*, 202–225.

Caumont, O., and V. Ducrocq (2008), What should be considered when simulating Doppler velocities measured by ground-based weather radars? *J. Appl. Meteor. Climatol*, *47*, 2256–2262.

Ferrier, B. S. (1994), A double-moment multiple-phase four-class bulk ice scheme. Part I: Description, *J. Atmos. Sci.*, *51*, 249–280.

Field, P. R., R. J. Hogan, P. R. A. Brown, A. J. Illingworth, T. W. Choularton, and R. J. Cotton (2005), Parameterization of ice-particle size distribution from mid-latitude stratiform cloud. *Q. J. R. Meteorol. Soc.*, *131*, 1997–2017.

Foote, G. B., and P. S. du Toit (1969), Terminal velocity of raindrops aloft, *J. Appl. Meteor.*, *8*, 249–253.

Gage, K. S., C. R. Williams, W. L. Clark, P. E. Johnston, and D. A. Carter (2002), Profiler contributions to Tropical Rainfall Measuring Mission (TRMM) ground validation field campaigns. *J. Atmos. Oceanic Technol.*, *19*, 843–863.

Gilmore, M. S., J. M. Straka, and E. N. Rasmussen (2004), Precipitation uncertainty due to variations in precipitation particle parameters within a simple microphysics scheme, *Mon. Wea. Rev.*, *132*, 2610–2627.

Han, M., S. A. Braun, W. S. Olson, P. O. G. Persson, and J.-W. Bao (2010), Application of TRMM PR and TMI measurements to assess cloud microphysical schemes in the MM5 for a winter storm, *J. Appl. Meteor. Climatol.*, *49*, 1129–1148.

Heymsfield, A. J., A. Bansemer, C. Schmitt, C. Twohy, and M. R. Poellot (2004), Effective ice particle densities derived from aircraft data, *J. Atmos. Sci.*, *61*, 982–1003.

Hogan, R. J., M. P. Mittermaier, and A. J. Illingworth (2006), The retrieval of ice water content from radar reflectivity factor and temperature and its use in evaluating a mesoscale model, *J. Appl. Meteor. Climatol.*, *45*, 301–317.

Hong, S.-Y., and J.-O. J. Lim (2006), The WRF single-moment 6-class microphysics scheme (WSM6), *J. Korean Meteor. Soc.*, *42*, 2, 129–151.

Houze, R. A. Jr., and S. Medina (2005), Turbulence as a mechanism for orographic precipitation enhancement, *J. Atmos. Sci.*, *62*, 3599−3623.

Iguchi, T., T. Matsui, J. J. Shi, W.-K. Tao, A. P. Khain, A. Hou, R. Cifelli, A. Heymsfield, and A. Tokay (2012), Numerical analysis using WRF-SBM for the cloud microphysical structures in the C3VP field campaign: Impacts of supercooled droplets and resultant riming on snow microphysics, *J. Geophys. Res.*, *117*, D23206, doi:10.1029/2012JD018101.

Kummerow, C. (1993), On the accuracy of the Eddington approximation for radiative transfer in the microwave frequencies, *J. Geophys. Res.*, *98*, 2757−2765.

Lang, S., W.-K. Tao, R. Cifelli, W. Olson, J. Halverson, S. Rutledge, and J. Simpson (2007), Improving simulations of convective systems from TRMM LBA: Easterly and westerly regimes, *J. Atmos. Sci.*, *64*, 1141–1164.

Lang, S. E., W.-K. Tao, X. Zeng, and Y. Li (2011), Reducing the biases in simulated radar reflectivities from a bulk microphysics scheme: Tropical convective systems, *J. Atmos. Sci.*, *68*, 2306–2320.

Li, X., W.-K. Tao, T. Matsui, C. Liu, and H. Masunaga (2010), Improving a spectral bin microphysical scheme using TRMM satellite observations, *Q. J. R. Meteorol. Soc.*, *136*, 382−399.

Lin, Y.-L., R. D. Farley, and H. D. Orville (1983), Bulk parameterization of the snow field in a cloud model, *J. Climate Appl. Meteor.*, *22*, 1065–1092.

Lin, Y., and B. A. Colle (2011), A new bulk microphysical scheme that includes riming intensity and temperature-dependent ice characteristics, *Mon. Wea. Rev.*, *139*, 1013–1035.

Liu, G. (2004), Approximation of single scattering properties of ice and snow particles for high microwave frequencies, *J. Atmos. Sci.*, *61*, 2441−2456.

Liu, C.-H., K. Ikeda, G. Thompson, R. Rasmussen, and J. Dudhia (2011), High-resolution simulations of wintertime precipitation in the Colorado Headwaters region: Sensitivity to physics parameterizations, *Mon. Wea. Rev.*, *139*, 3533–3553.

Locatelli, J. D., and P. V. Hobbs (1974), Fall speeds and masses of solid precipitation particles, *J. Geophys. Res.*, *79*, 2185–2197.

McFarquhar G. M., and A. J. Heymsfield (1996), Microphysical characteristics of three anvils sampled during the central equatorial Pacific experiment, *J. Atmos. Sci.*, *53*, 2401–2423.

Masunaga, H., and et al. (2010), Satellite Data Simulator Unit: A multisensory, multispectral satellite simulator package, *Bull. Amer. Meteor. Soc.*, *91*, 1625–1632.

Matsui, T., X. Zeng, W.-K. Tao, H. Masunaga, W. S. Olson, and S. Lang (2009), Evaluation of long-term cloud-resolving model simulations using satellite radiance observations and multifrequency satellite simulators, *J. Atmos. Oceanic Technol.*, *26*, 1261–1274.

Molthan, A., and B. Colle (2012), Comparisons of single and double-moment microphysics schemes in the simulation of a synoptic-scale snowfall event, *Mon. Wea. Rev. 140*, 2982−3002.

Milbrandt, J. A., and M. K. Yau (2005), A multimoment bulk microphysics parameterization. Part II: A proposed three-moment closure and scheme description, *J. Atmos. Sci.*, *62*, 3065−3081.

Milbrandt, J. A., M. K. Yau, J. Mailhot, and S. Belair (2008), Simulation of an orographic precipitation event during IMPROVE-2. Part I: Evaluation of the control run using a triple-moment bulk microphysics scheme, *Mon. Wea. Rev.*, *136*, 3873−3893.

Morrison, H., J. A. Curry, and V. I. Khvorostyanov (2005), A new double-moment microphysics parameterization for application in cloud and climate models. Part I: Description, *J. Atmos. Sci.*, *62*, 1665–1677.

Morrison, H., G. Thompson, and V. Tatarskii (2009), Impact of cloud microphysics on the development of trailing stratiform precipitation in a simulated squall line: Comparison of one- and two- moment schemes, *Mon. Wea. Rev.*, *137*, 991–1007.

Neiman, P. J., F. M. Ralph, G. A. Wick, J. D. Lundquist, and M. D. Dettinger (2008), Meteorological characteristics and overland precipitation impacts of atmospheric rivers affecting the west coast of North America based on eight years of SSM/I satellite observations, *J. Hydrometeor.*, *9*, 22–47.

Olson, W. S., P. Bauer, C. D. Kummerow, Y. Hong, and W.-K. Tao (2001), A melting-layer model for passive/active microwave remote sensing applications. Part II: Simulations of TRMM observations, *J. Appl. Meteor.*, *40*, 1164–1179.

Ralph, F. M., P. J. Neiman, G. N. Kiladis, K. Weickmann, and D. W. Reynolds (2011), A multiscale observational case study of a Pacific atmospheric river exhibiting Tropical-Extratropical connections and a mesoscale frontal wave, *Mon. Wea. Rev.*, *139*, 1169–1189.

Rutledge, S. A., and P. V. Hobbs (1983), The mesoscale and microscale structure and organization of clouds and precipitation in midlatitude cyclones. VIII: A model for the "seeder-feeder" process in warm-frontal rainbands, *J. Atmos. Sci.*, *40*, 1185–1206.

Smith, P. L. (1984), Equivalent radar reflectivity factors for snow and ice particles, *J. Climate Appl. Meteor.*, *23*, 1258–1260.

Smith, B. L., S. E. Yuter, P. J. Newman, and D. E. Kingsmill (2010), Water vapor fluxes and orographic precipitation over northern California associated with a landfalling atmospheric river, *Mon. Wea. Rev.*, *138*, 74–100.

Solomon, A., H. Morrison, O. Persson, M. D. Shupe, and J.-W. Bao (2009), Investigation of microphysical parameterization of snow and ice in Arctic clouds during M-PACE through model-observation comparisons, *Mon. Wea. Rev.*, *137*, 3110–3128.

Spencer, R. W., H. M. Goodman, and R. E. Hood (1989), Precipitation retrieval over land and ocean with the SSM/I: Identification and characteristics of the scattering signal, *J. Atmos. Oceanic Technol.*, *6*, 254–273.

Shi, J. J., W.-K. Tao, T. Matsui, A. Hou, S. Lang, C. Peters-Lidard, G. Jackson, R. Cifelli, S. Rutledge, and W. Petersen (2010), Microphysical Properties of the January 20-22 2007 Snow Events over Canada: Comparison with in-situ and Satellite Observations, *J. Appl. Meteor. Climatol. 49*, 2246–2266.

Tao, W.-K., and J. Simpson (1993), Goddard cumulus ensemble model. Part I: Model description, *Terr. Atmos. Oceanic Sci.*, *4*, 35–72.

Tao, W.-K., et al. (2003), Microphysics, radiation and surface processes in the Goddard Cumulus Ensemble (GCE) model, *Meteor. Atmos. Phys.*, *82*, 97–137.

Tao, W.-K., J. J. Shi, S. S. Chen, S. Long, P.-L. Lin, S.-Y. Hong, C. P.-L., and S. Hou (2011), The impact of microphysical schemes on hurricane intensity and track, *Asia-Pacific J. Atmos. Sci.*, *47*(1), 1–16.

Thompson G., P. R. Field, R. M. Rasmussen, and W. D. Hall (2008), Explicit forecasts of winter precipitation using an improved bulk microphysics scheme. Part II: Implementation of a new snow parameterization, *Mon. Wea. Rev.*, *136*, 5095–5115.

Tian, L., G. M. Heymsfield, A. J. Heymsfield, A. Bansemer, L. Li, C. H. Twohy, and R. C. Srivastava (2010), A study of cirrus ice particle size distribution using TC4 observations, *J. Atmos. Sci.*, *67*, 195–216.

Tong M., and M. Xue (2005), Ensemble Kalman filter assimilation of Doppler radar data with a compressible nonhydrostatic model: OSS experiments, *Mon. Wea. Rev.*, *133*, 1789–1807.

White, A. B., J. R. Jordan, B. E. Martner, F. M. Ralph, and B. W. Bartram (2000), Extending the dynamic range of an S-band radar for cloud and precipitation studies, *J. Atmos. Oceanic Technol.*, *17*, 1226–1234.

White, A. B., D. J. Gottas, E. T. Strem, F. M. Ralph, and P. J. Neiman (2002), An automated brightband height detection algorithm for use with Doppler radar spectral moments, *J. Atmos. Oceanic Technol.*, *19*, 687–697.

Williams, C. R., W. L. Ecklund, and K. S. Gage (1995), Classification of precipitating clouds in the Tropics using 915-MHz wind profilers, *J. Atmos. Oceanic Technol.*, *12*, 996–1012.

Williams, C. R., K. S. Gage, W. L. Clark, and P. A. Kucera (2005), Monitoring the reflectivity calibration of a scanning radar using a profiling radar and a disdrometer, *J. Atmos. Oceanic Technol.*, *22*, 1004–1018.

Williams, C. R., A. B. White, K. S. Gage, and F. M. Ralph (2007), Vertical structure of precipitation and related microphysics observed by NOAA profilers and TRMM during NAME 2004, *J. Climate*, *20*, 1693–1712.

Zupanski, D., S. Q. Zhang, M. Zupanski, A. Y. Hou, and S. H. Cheung (2011), A prototype WRF-based ensemble data assimilation system for dynamically downscaling satellite precipitation observations, *J. Hydrometeor*, *12*, 118–134.